3-2004

Magnetogasdynamic Flow Control of a Mach Reflection

Brian E. Earp

MAGNETOGASDYNAMIC FLOW CONTROL
OF A MACH REFLECTION

THESIS

Brian E. Earp, Captain, USAF

AFIT/GAE/ENY/04-M07

DEPARTMENT OF THE AIR FORCE

AIR UNIVERSITY

AIR FORCE INSTITUTE OF TECHNOLOGY

Wright-Patterson Air Force Base, Ohio

AFIT/GAE/ENY/04-M07

MAGNETOGASDYNAMIC FLOW CONTROL
OF A MACH REFLECTION

THESIS

Presented to the Faculty of the

Department of Aeronautics and Astronautics

Graduate School of Engineering and Management

Air Force Institute of Technology

Air University

Air Education and Training Command

in Partial Fulfillment of the Requirements for the

Degree of Master of Science in Aeronautical Engineering

Brian E. Earp, B.S.

Captain, USAF

March, 2004

AFIT/GAE/ENY/04-M07

MAGNETOGASDYNAMIC FLOW CONTROL

OF A MACH REFLECTION

Brian E. Earp, B.S.

Captain, USAF

Approved:

_____	_____
Maj Richard J. McMullan, Ph.D.	Date
Thesis Advisor	
_____	_____
Lt Col Montgomery C. Hughson, Ph.D.	Date
Committee Member	
_____	_____
Lt Col Raymond C. Maple, Ph.D.	Date
Committee Member	

AFIT/GAE/ENY/04-M07

Abstract

   Two-dimensional regular and Mach reflections have been studied in the Mach 4.96 dual-solution domain for a 25° and 26° double-fin inlet. The steady-state computational Mach and regular reflections were subjected to magnetogasdynamic forces to determine whether these forces could be used as a possible flow control mechanism. The numerical code employed for this research solved the inviscid Euler equations with added source terms for the ponderomotive force and accompanying energy interactions. The 25° regular reflection was determined to be extremely sensitive to a decelerating Lorentz force. Transient application of the force led to the transition of the regular reflection to a Mach reflection, increasing the total pressure losses and decreasing the compression ratio. Sustained application of the force resulted in inlet unstart. An accelerating Lorentz force was also examined with the goal of transitioning the 26° Mach reflection to a more efficient regular reflection. The location of the accelerating force and the parameters governing its magnitude were examined. Such forces push the Mach reflection back to a more stable location and reduce the Mach stem height. For the interaction parameters considered, fully regular reflections were not obtained. However, the accelerating Lorentz force proved capable of increasing the total pressure recovery and the static pressure compression beyond the regular reflection values.

iv

Acknowledgements

First, I thank my advisor, Maj Jeff McMullan. It was a long and arduous process and without his help, I might not have finished it. His continuous guidance and patience were a lesson for me as a future instructor and an Air Force officer. I acknowledge the members of my committee Lt Col Monty Hughson and Lt Col Ray Maple for their help in completing the task. The final product is complete due to their input. Without Lt Col Maple's expertise, the data would still be locked behind many computer problems. I thank Dr. Datta Gaitonde for his support and knowledge. Any question was promptly answered in a way I could fathom, and explain myself. The support and background work provided by Dr. J. Schmisseur and AFRL/VAAC created a foundation on which I could build a thesis. Most of all, I thank my family and Marie. Without their love, support, and encouragement, I would not have made it to the finish, or even started the race.

I am grateful for the AFRL/VAAC grant and AFOSR sponsorship under the tasks monitored by Drs. J. Schmisseur, W. Hilbun, and F. Fahroo.

<div align="right">Brian E. Earp</div>

Table of Contents

List of Figures

List of Tables

List of Symbols

Roman symbols:

A	Flux Jacobian of the ξ flux, $\frac{\partial \hat{\mathbf{E}}}{\partial \hat{U}}$ or area
a	sound speed
B	magnetic flux density or Flux Jacobian of the η flux, $\frac{\partial \hat{\mathbf{F}}}{\partial \hat{U}}$
B_0	magnitude of the magnetic flux density
C	Flux Jacobian of the ζ flux, $\frac{\partial \hat{\mathbf{G}}}{\partial \hat{U}}$
c_p	constant pressure specific heat
D	electric flux density
E	electric field or viscous/inviscid component of the flux vector in the x- or ξ-direction
E_0	magnitude of the applied electric field
$\mathbf{E}$	flux vector in the x- or ξ-direction
e	energy
F	viscous/inviscid component of the flux vector in the y- or η-direction
$\mathbf{F}$	flux vector in y- or η-direction
f	force density
G	viscous/inviscid component of the flux vector in the z- or ζ-direction
$\mathbf{G}$	flux vector in z- or ζ-direction
g	half throat diameter
H	magnetic field or Roe averaged enthalpy
h	enthalpy
J	Jacobian of transformation
j	conduction current density
$\mathcal{K}$	load factor
k	cell interface area
L	reference length
M	Mach number
Mm	magnetic Mach number

Pm	magnetic Prandtl number
Pr	Prandtl number
p	pressure
$\mathcal{Q}$	interaction parameter
q	heat flux
R	Roe density ratio
$\mathbf{R}$	residual vector
Re	Reynolds number
Rm	magnetic Reynolds number
r	ratios for variable extrapolation
S	source vector or Sutherland's Law Constants
T	temperature
t	time
U	conservative variable vector
$\mathcal{U}$	contravariant velocity in ξ-direction
u	component of velocity in the x-direction
V	velocity
$\mathbf{V}$	primitive variable vector
$\mathcal{V}$	contravariant velocity in η-direction
v	component of velocity in the y-direction
$\mathcal{W}$	contravariant velocity in ζ-direction
w	component of velocity in the z-direction or compression ramp length
x	coordinate direction of the principle axis
y	coordinate direction of the principle axis
z	coordinate direction of the principle axis

Greek symbols:

α Roe vector quantities

β oblique shock angle

γ ratio of specific heats

Δ difference operator

δ differential operator or conductivity pattern constant

δ_{99} boundary layer thickness

δ_{ij}, δ_{ji} Kronecker delta

ϵ permittivity

ζ generalized coordinate

η generalized coordinate

Θ_B surface angle

θ compression ramp angle

θ_d von Neumann ramp angle

θ_N detachment ramp angle

κ thermal conductivity or variable extrapolation constant

λ eigenvalue

μ permeability or viscosity

ν kinematic viscosity

ξ generalized coordinate

ρ density

ρ_e charge unit volume

σ conductivity

τ stress tensor or generalized time

Φ variable extrapolation constant

ϕ temporal integration order of accuracy

∂ partial differential operator

∇ gradient operator

Subscripts:

0	freestream value or reference location
$1, 2, 3, 4, 5, 6, 7, 8$	Roe vector indices
$\pm\frac{1}{2}$	interface
∞	freestream value
bs	quantity behind the shock
e	electromagnetic
f	fluid
i	inviscid, index notation, tensorial component, or inlet condition
j, k	index notation or tensorial component
L	left cell interface
ni, nj, nk	maximum index
R	right cell interface
t	total condition
v	viscous
x	x-component or differentiation with respect to x
y	y-component or differentiation with respect to y
z	z-component or differentiation with respect to z
ζ	differentiation with respect to ζ
η	differentiation with respect to η
ξ	differentiation with respect to ξ
τ	differentiation with respect to τ

Superscripts:

n time level

p sub-iteration counter

$\pm$ forward and backward quantities

$'$ rest frame

$*$ dimensionless quantity

$\rightarrow$ vector quantity

$\hat{}$ vectors in generalized coordinates

$\longrightarrow$ vector quantity

$\bar{}$ average value

$\tilde{}$ Roe averaged values

$\tilde{\bar{}}$ Roe averaged average value

Constants:

$\mathbf{c}$	speed of light *in vacuo*	$2.998 \times 10^8 \frac{m}{s}$
$\mathcal{R}$	universal gas constant	$287 \frac{J}{kgK}$
S_{κ_f}	Sutherland's Law thermal conductivity temperature constant	194 K
S_{μ_f}	Sutherland's Law molecular viscosity temperature constant	111 K
$\kappa_{0,f}$	Sutherland's Law thermal conductivity constant for air	$2.41 \times 10^{-2} \frac{W}{mK}$
$\epsilon_{0,e}$	electric constant (permittivity of free space)	$8.854 \times 10^{-12} \frac{F}{m}$
$\mu_{0,e}$	magnetic constant (permeability of free space)	$4\pi \times 10^{-7} \frac{H}{m}$
$\mu_{0,f}$	Sutherland's Law molecular viscosity constant for air	$1.716 \times 10^{-5} \frac{Ns}{m^2}$

List of Abbreviations

MAGNETOGASDYNAMIC FLOW CONTROL
OF A MACH REFLECTION

1. Introduction

Starting with the first flight of a powered aircraft on 17 December 1903 by Orville and Wilbur Wright, mankind's continuing desire to fly "faster and higher"[1] has pushed the limit of aircraft and spacecraft design. These aspirations have led to many new performance achievements, from the first hypersonic flight of the modified two-stage V-2 rocket in 1949[1] to the Space Shuttle Columbia's first manned/winged vehicle re-entry flight[12]. Figure 1.1 depicts a few of the milestones of high-speed flight in the past century. These milestones have helped pave the way in hypersonic flight, leading towards the ultimate goal of sustained hypersonic flight whereby one could fly from New York to Tokyo in as little as two hours[1]. The cost of putting a payload in space could be reduced by 1-to-2 orders of magnitude with a single-stage-to-orbit (SSTO) hypersonic aerospace vehicle.

Hypersonic flight can be achieved with rocket or air-breathing propulsion. Rocket propulsion, both solid- and liquid-fuelled, is the current means for hypersonic travel. Over the past fifty years, many missiles, aircraft, and spacecraft have been propelled to hypersonic velocities, greater than Mach 5, by rocket engines. However, the objective of sustained hypersonic flight, manned or unmanned, drives propulsion designers toward an air-breathing propulsion source. Air-breathing engines use atmospheric oxygen instead of carrying an oxidizer. Subsequently, the payload and/or the range of the hypersonic vehicle increases. Therefore, hypersonic transports could
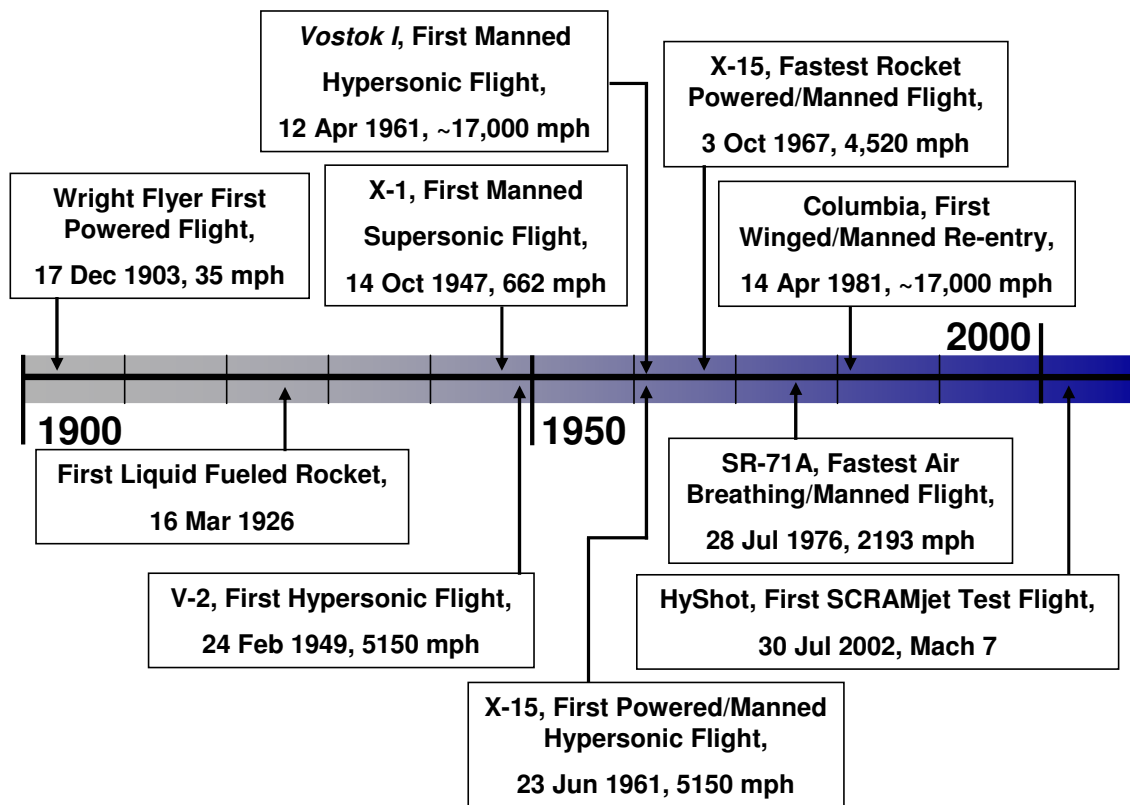
Figure 1.1   Time-line of major hypersonic and space flight events[1, 12, 16, 21, 24]

carry a greater payload for longer distances, and hypersonic missiles could project larger warheads over a greater range when the internal oxidizer is removed.

One of the air-breathing propulsion types studied for hypersonic flight is the supersonic combustion ramjet (SCRAMjet). Figure 1.2 depicts the National Air and Space Administration's (NASA) X-43A[21]. The X-43A is an unmanned hypersonic vehicle which uses a SCRAMjet to fly between Mach = 7 and 10. The vehicle is boosted to Mach 7 by a Pegasus solid-rocket motor and then separates from the rocket and ignites the SCRAMjet. The first X-43A flight was lost in June of 2002 due to problems caused by the solid-rocket booster.

The X-43 demonstrates many of the key features of a SCRAMjet engine. The initial compression and slowing of the flow is due to the bottom surface of the aircraft as depicted in Fig. 1.2. This surface acts as a compression ramp creating
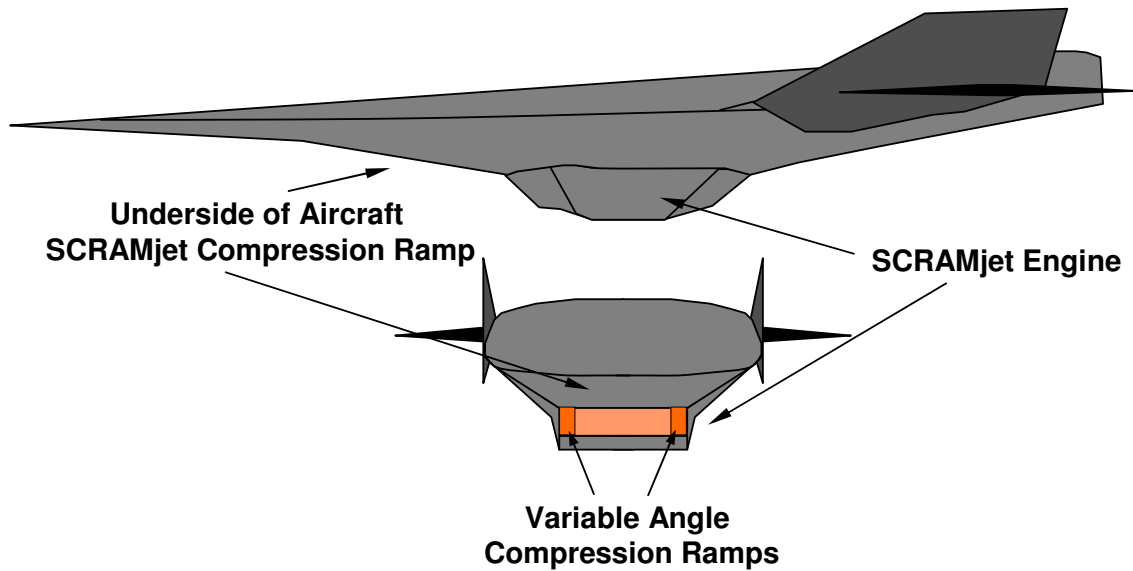
Figure 1.2   Schematic of the X-43A hypersonic vehicle [NASA]

an oblique shock ending on the lower lip of the inlet[2]. The flow then goes through a complex set of oblique shocks created by the variable angle compression ramps in the inlet of the engine. These ramps are adjusted to the angle required to create the proper compression for the flight condition. The supersonic mixing and combustion of the fuel occurs in the combustor section. The resulting high-temperature gases are expanded through the nozzle and ejected out the rear of the engine[10]. The exhaust gases are further expanded to freestream pressure using both the bottom surface of the aircraft behind the engine and the pressure difference of the freestream flow[2]. This sequence of events is controlled completely by the variable ramps and the injection of fuel.

The complex shock wave interactions present in internal flowfields influence the design and performance of SCRAMjet engines. The shock waves interact with each other and the turbulent boundary layers on the adjacent walls creating complex shock-shock and shock-boundary layer structures. This highly non-linear phenomenon can induce separation in the boundary layer and extreme deformation in the flowfield. These effects lead to total pressure losses, reduced performance, and

possible engine unstart where the shock system is expelled from the inlet. These potential problems drive researchers and designers to attempt to understand and control the complex interaction phenomena.

The complicated geometry of a SCRAMjet inlet has been modelled recently as shown in Fig. 1.3[17, 20, 29, 30]. This model is composed of a flat plate, representing the underside of the aircraft compression ramp in Fig. 1.2, and perpendicular shock generators on each side of the flat plate. The oblique shock generated by the underside of the aircraft is taken into account by the freestream conditions entering the inlet, while the flat plate simply grows a boundary layer which induces shock-boundary layer interactions. The shock generators can be adjusted to any angle θ to change the angles of the oblique shocks, β, and the corresponding flow compression of the inlet.

1.1 Regular and Mach Reflections

When $M_\infty = 4.96$, there exists an essentially two-dimensional (2-D) region for this double-fin configuration beginning 27 boundary layer thickness above the flat plate[29]. In order to investigate this region, a 2-D domain is created from a single slice of the three-dimensional (3-D) model in Fig. 1.3. The slice, shown in Fig. 1.4, is used to calculate the interactions of the oblique shocks without the influence of the boundary layer of the flat plate. In agreement with theory, experimental and computational results show that either a regular reflection or a Mach reflection can exist at these conditions when θ is between 22° and 28° [13, 14, 17, 20, 29, 30].

A regular reflection (RR) is characterized by oblique shocks off the leading edges of the fins at the angle specified by oblique shock theory. The shock angle, β, is a function of the freestream Mach number and the compression angle, θ. Figure 1.5 shows the RR generated by a double fin configuration with $\theta = 25^o$ and $M_\infty = 4.96$. At the intersection of the primary oblique shocks generated by each fin, the shocks reflect in a regular fashion. Expansion fans form at the throat of the inlet and interact with the reflected oblique shocks inducing curvature towards the walls. The
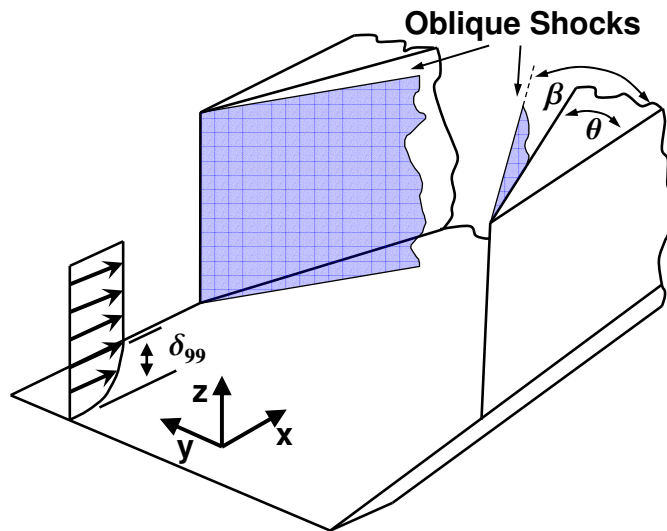
Figure 1.3   Schematic of the double-fin generated crossing shock-wave turbulent
             boundary-layer interaction
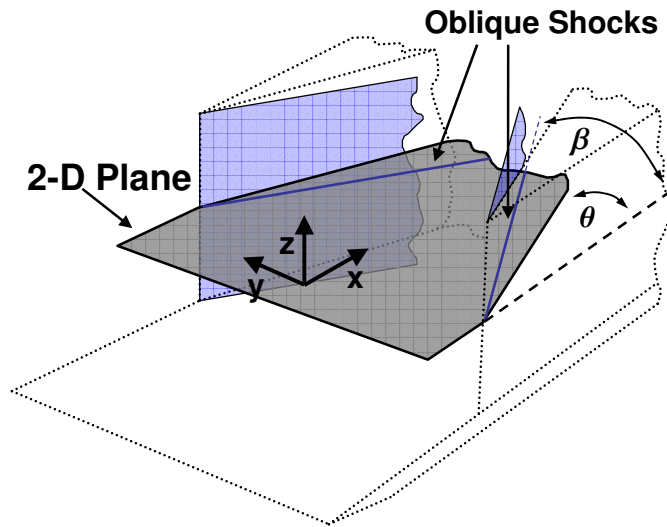
Figure 1.4   Schematic of the 2-D slice from the double-fin configuration turbulent
             boundary-layer interaction

oblique shocks continue to reflect off the walls and each other as the flow continues through the inlet until they exit the channel as illustrated by Fig. 1.5.
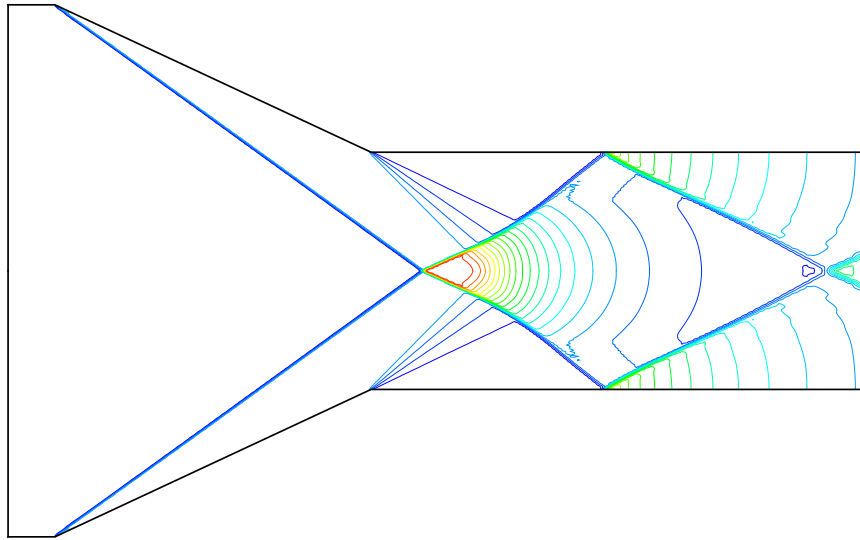
Figure 1.5   Pressure contours from a regular reflection for $M_\infty = 4.96$, 2-D solutions, $25^o \times 25^o$

The Mach reflection (MR) for the equivalent conditions has oblique shocks coming off the leading edges of the fins identical to the regular reflection. However, a normal shock (Fig. 1.6) is formed between the two oblique shocks instead of the oblique shock to shock reflection. The size of the normal shock is a is determined by the freestream Mach number and fin angles. This normal shock is also known as the Mach stem.

The region behind the MR is characterized by a slip-line between the subsonic flow behind the normal shock and the supersonic flow behind the reflected oblique shocks as shown in Fig. 1.7. The large region of subsonic flow decreases the inlet
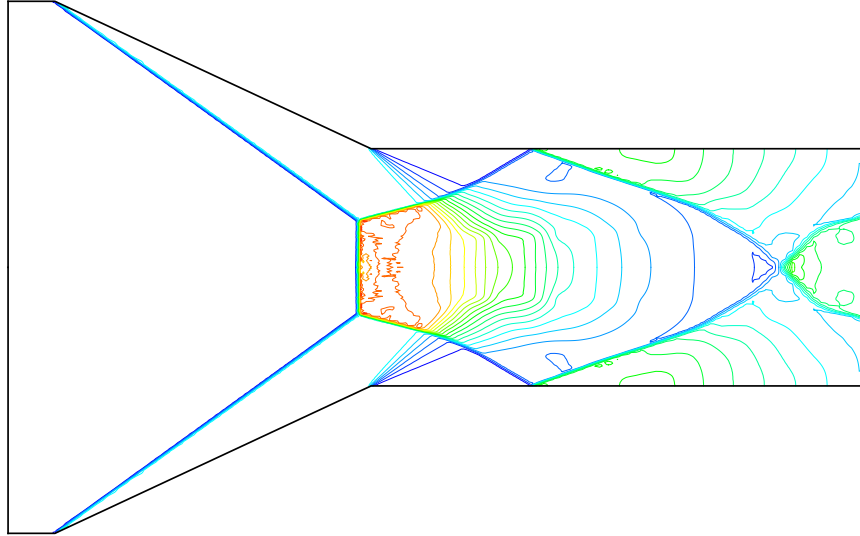
Figure 1.6   Pressure contours from a Mach reflection for $M_\infty = 4.96$, 2-D solutions, $25^o \times 25^o$

efficiency and increases the total pressure losses. This Mach reflection could occur in the inlet due to changes in the performance of the propulsion system at off-design flight conditions.

Whether the flow develops a RR or a MR is dependent on the pressure rise across the oblique shocks[13, 14]. The von Neumann angle, θ_N, is the wedge angle for a given freestream condition where the pressure rise across the initial and reflected oblique shocks is equal to the pressure rise across a single normal shock. The detachment angle, θ_d, is the wedge angle for a given freestream condition when the initial oblique shock waves are too strong for the reflected oblique shock waves to remain attached to each other. Ramp angles less than θ_N form regular reflections and ramp angles greater than θ_d form Mach reflections. The range of wedge angles

Slip-lines between Subsonic and Supersonic Flow
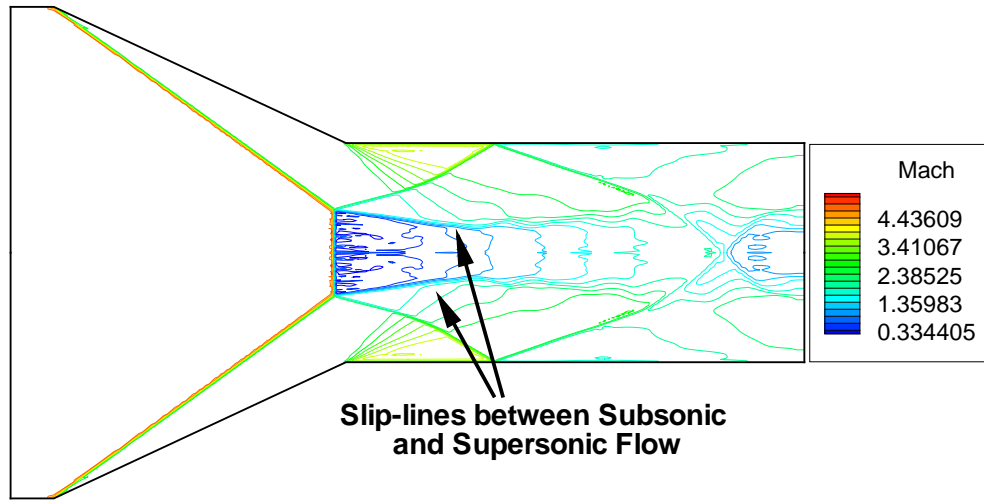
Figure 1.7   Isobars of Mach number from a Mach reflection for $M_\infty = 4.96$, 2-D solutions, $25^o \times 25^o$

between θ_N and θ_d for a given freestream Mach number is known as the dual-solution domain where both a RR and a MR can exist[13, 14].

The inlet ramp angles are adjusted to a specific θ to produce a set of oblique shocks with the proper inlet compression ratio. The required compression ratio is based on the flight condition and the throttle position. A MR produces a lower compression ratio resulting in reduced thrust. In addition, normal shocks have greater losses in total pressure across them than oblique shocks. Therefore, the MR condition has higher total pressure losses and lower inlet efficiency than the corresponding RR as shown in Fig. 1.8. These large total pressure losses associated with the nor-

mal shock in the Mach reflection can lead to an unstart of the engine inlet.[9] The consequences of engine unstart include a loss in the total pressure recovery, dramatic increases in drag, and potential loss of aircraft control.
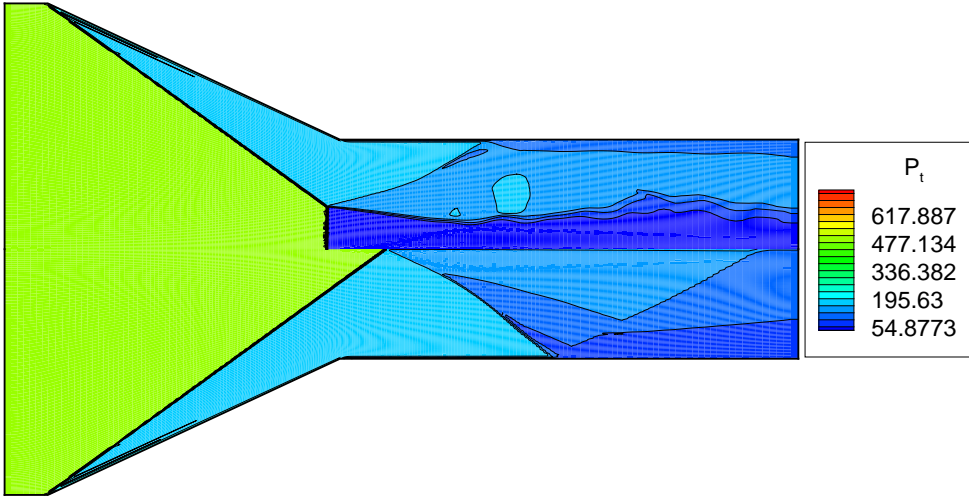
Figure 1.8   Mach and Regular reflection total pressure comparison for $M_\infty = 4.96$, 2-D solutions, $25^o \times 25^o$

1.2   Previous Research

Extensive research has been performed by several researchers on this dual-solution domain[17, 20, 29, 30, 34]. The research includes numerical simulations and experiments for both two- and 3-D configurations. The 3-D computations and experiments explore the shock-shock and shock-boundary layer interactions, and how these interactions affect each other. Although the 3-D research has been conducted

in the dual-solution domain, these simulations and experiments have not been able to demonstrate a regular reflection, resolving a Mach reflection in every case[17, 18, 20, 29, 30]. This is attributed to the boundary layer's effect on the oblique shock interaction and the accompanying change in the flowfield. However, the 2-D computations and experiments have demonstrated both solutions[30, 18].

Figure 1.9 is the schematic of Schmisseur and Gaitonde's 2-D solution domain[30]. The 2-D slice in Fig. 1.4 is cut in half with a symmetry boundary condition down the center to reduce the number of cells and corresponding computation time. Their computational solutions employed compression angles of $22^o \leq \theta \leq 28^o$ at a freestream $M_\infty = 4.96$ and Reynolds number based on w of 2 million. These conditions correspond to those at which experimental data were obtained by Ivanov, et al. [17, 20] in order to facilitate validation of both Navier-Stokes and Euler simulations.
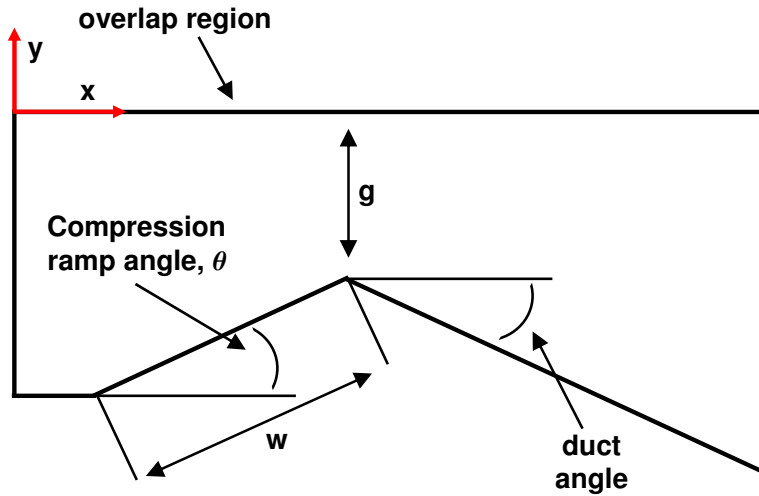
Figure 1.9   Schematic of Schmisseur and Gaitonde's 2-D physical domain[30]

The hysteresis phenomenon shown in Fig. 1.10 was simulated by Schmisseur and Gaitonde for inlet conditions with $g/w = 0.42$ and $g/w = 0.34$[30]. The half throat diameter is defined g and w is the length of the compression surface as shown in Fig. 1.9. For the $g/w = 0.34$ results in the dual-solution domain, the compression angle was incrementally increased from the theoretical von Neumann condition, $\theta_N = 20.87^o$. The transition from RR to MR occurred at a compression angle between

27.5^o and 27.85^o. This angle range is in close agreement with the theoretical value for detachment, $\theta_d = 27.7^o$. Once a MR solution was obtained, the solution was used as the initial condition for solution of the lower compression angle. The MR pattern persisted through much of the dual-solution space transitioning to an RR configuration before the von Neumann condition was reached. The transition from a MR to RR solution occurred between $\theta = 22^o$ and 23°. The inviscid numerical results for the height of the normal shock Mach stem of Schmisseur and Gaitonde[30] showed good agreement with the experimental data and Euler solutions by Ivanov, et al. [20] as shown in Fig. 1.11. This figure indicates particularly good agreement in the region of the dual-solution domain near detachment. In this region the experimental data generally lie within the mesh resolution of the numerical values.
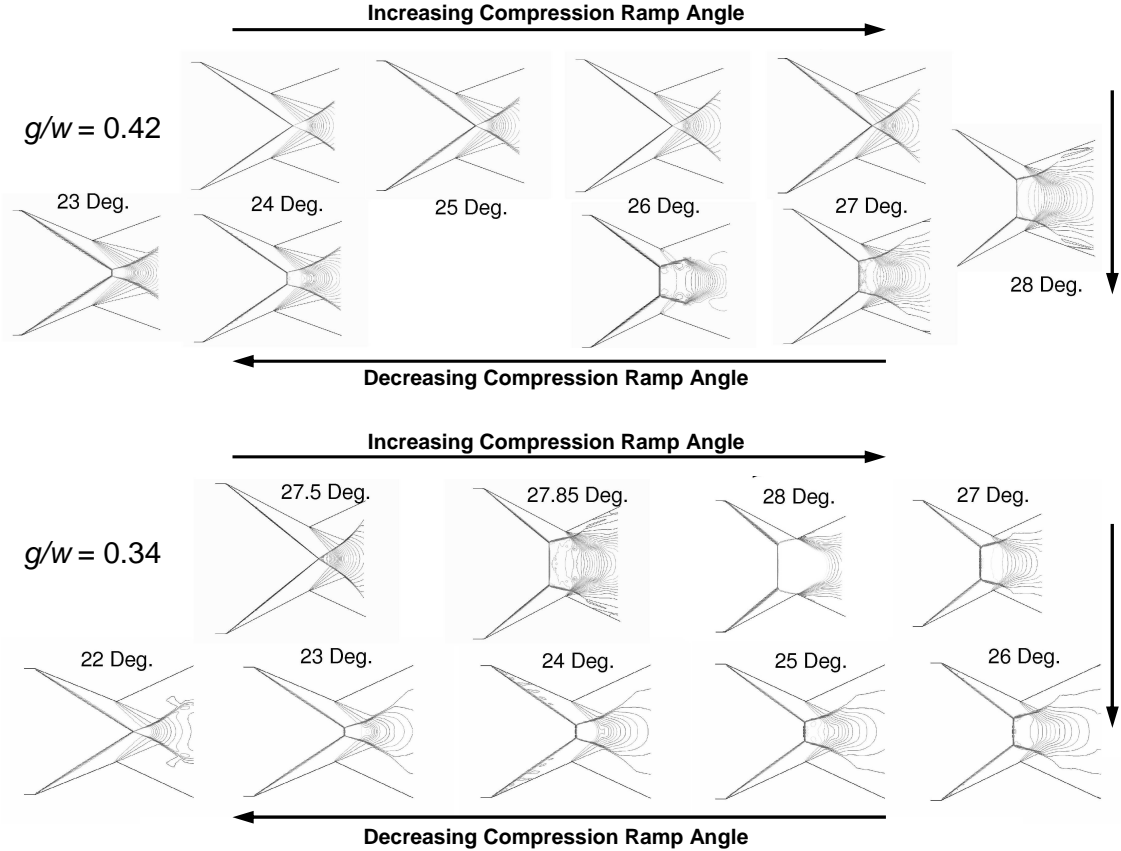
Figure 1.10   Hysteresis loop for Mach 5, 2-D solutions[30]
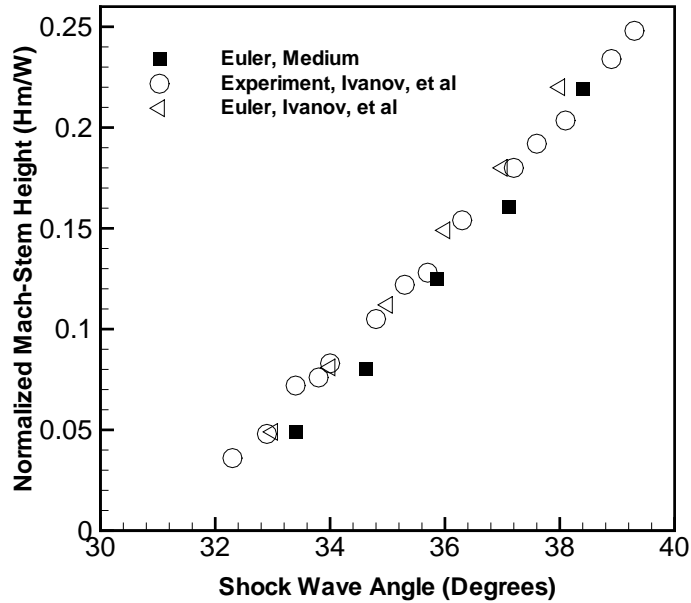
Figure 1.11   Variation of Mach-stem height with θ for 2-D solutions[30] (Medium corresponds to a grid resolution of $206 - 329 \times 137$)

Ivanov, et al. produced the hysteresis experimentally for a freestream Mach of 4[?]. The results demonstrated the dual-solution domain from $\theta = 34^o$ to $\theta = 38.2^o$. These values are very close to the von Neumann and detachment angles for $M_\infty = 4$ of 33.4^o and 39.2^o, respectively.

Since the transition from regular reflection to Mach reflection can initiate many problems, control and/or prevention of this flowfield transition is an obvious goal. Researchers have examined the factors which transition the flow and methods of controlling the transition[13, 14, 19, 34, 35]. The experiments of Yan, et al. with laser energy deposition have successfully transitioned a RR to MR and a MR to RR[34, 35]. This method energizes the flow in front of the shock system. In the current research, magnetogasdynamics is investigated as a method of controlling this flow transition.

1.3 Magnetogasdynamics

Magnetofluidmechanics (MFD) unifies electrodynamics, thermodynamics, and fluid mechanics into one discipline, the study of the interaction between electromagnetic fields and a continuum fluid[15]. These interactions can be modelled by coupling the Maxwell equations with the Navier-Stokes equations. Magnetogasdynamics (MGD) is the subset of MFD associated with continuum gases and the many environmental variables present in hypersonic flight. Applying MFD to the hypersonic flight regime allows many simplifying assumptions to be made. The induced magnetic field is negligible for low magnetic Reynolds number flows. The flow is weakly ionized so the conductivity is low. The low conductivity specifies a magnetic Reynolds number much less than 1. This simplification allows the use of the low magnetic Reynolds number form of the governing equations. The MGD source terms that remain are the ponderomotive forces and accompanying energy interaction terms[15].

In recent years, magnetogasdynamics has been suggested as a flow control mechanism for the hypersonic flow regime[5, 7, 8, 22, 23, 25]. Researchers have examined the use of electromagnetic fields to control shock location for inlet mass-capture, enhance fuel-air mixing, suppress boundary layer transition, and serve as a means to efficiently withdraw energy from the flow in the inlet and add energy to the flow in the nozzle for thrust enhancement. The primary mechanisms are ponderomotive, or Lorentz, forces and accompanying energy interactions, which include both reversible and irreversible components. The potential use of MGD to transition a SCRAMjet inlet from Mach reflection to regular reflection is an enticing prospect. In theory, a Lorentz force applied tangent to the flow could be used to reduce or even eliminate the MR. This application of the Lorentz force reduces the normal shock stem height, helps to sustain supersonic combustion, and minimizes the chance of engine unstart. The same applied force could also prevent transition to MR before it could occur.

1.4 Current Research

The current research effort begins with the regular and Mach reflection data of Schmisseur and Gaitonde[30] and applies magnetogasdynamic forces to determine the sensitivity of both types of reflections to decelerating and accelerating Lorentz forces. A 2-D inviscid inlet is examined at multiple compression ramp angles in the dual-solution domain. A converged RR is subjected to a decelerating Lorentz force to determine its sensitivity to transition to a MR and possible unstart. In addition, an accelerating Lorentz force is applied to a MR to try and transition the MR to a more efficient RR.

This numerical study employs a 3-D magnetogasdynamic Computational Fluid Dynamics (CFD) code[3, 4, 5, 6, 7, 8]. The code was written by the Computational Branch of the Aerodynamics Division of the Air Vehicles Directorate (VAAC) within the Air Force Research Laboratory (AFRL). The code solves the Euler or Navier-Stokes equations with the addition of source terms for the MGD forces and energy interactions. The AFRL/VAAC code has been verified for various problems including 2-D flow past a flat plate and a laminar MGD boundary layer flow[5, 7]. For the current research, the inviscid Euler equations are solved.

The magnetogasdynamic governing equations used in this research are developed in Section 2 from the Navier-Stokes equations and the Maxwell equations. In section 3, the numerical algorithms used to solve the magnetogasdynamic equations are presented. Section 3 also includes a detailed explanation of the the computational domain set-up for this research. Section 4 begins with duplication of Schmisseur and Gaitonde's hysteresis. The sensitivity of the regular reflection to a decelerating Lorentz force and the Mach reflection to an accelerating Lorentz force are examined, including the dependency on location of the applied field and the magnitude of the applied magnetic and electric fields. Section 5 presents some conclusions on the use of MGD to control Mach reflections and possible future work.

2. Governing Equations

2.1 Navier-Stokes Equations

The Navier-Stokes equations (NSE) are the governing equations of fluid flow. These equations are based on the laws of the conservation of mass, momentum, and energy. When radiative heat transfer and body forces are neglected, these laws can be expressed as the continuity, momentum, and energy equations below:

$$\frac{\partial \rho}{\partial t} + \frac{\partial (\rho V_j)}{\partial x_i} = 0 \tag{2.1}$$

$$\frac{\partial (\rho V_i)}{\partial t} + \frac{\partial (\rho V_i V_j)}{\partial x_j} = \frac{\partial (p \delta_{ij})}{\partial x_j} + \frac{\partial \tau_{ij}}{\partial x_j} \tag{2.2}$$

$$\frac{\partial (\rho e_t)}{\partial t} + \frac{\partial (\rho h_t V_j)}{\partial x_j} = \frac{\partial (q_j + \tau_{ji} V_i)}{\partial x_j} \tag{2.3}$$

The velocity vector, $\vec{V}$, is composed of u, v, and w components in the x-, y-, and z-cartesian directions, respectively. V_i, V_j, or V_k represents one of these components. The stress tensor, τ_{ij}, and the heat flux vector, q_j, are defined below:

$$\tau_{ij} = \mu_f \left(\frac{\partial V_i}{\partial x_j} + \frac{\partial V_j}{\partial x_i} \right) - \frac{2}{3} \delta_{ij} \mu_f \frac{\partial V_k}{\partial x_k} \tag{2.4}$$

$$q_j = \kappa_f \frac{\partial T}{\partial x_j} \tag{2.5}$$

Sutherland's Law determines the molecular viscosity, μ_f, and thermal conductivity, κ_f, based on local temperature as follows:

$$\mu_f \approx \mu_{0,f} \left(\frac{T}{T_0} \right)^{\frac{3}{2}} \frac{T_0 + S_{\mu_f}}{T + S_{\mu_f}} \tag{2.6}$$

$$\kappa_f \approx \kappa_{0,f} \left(\frac{T}{T_0}\right)^{\frac{3}{2}} \frac{T_0 + S_{\mu_f}}{T + S_{\kappa_f}} \tag{2.7}$$

where $\mu_{0,f} = 1.716 \times 10^{-5}$, $T_0 = 273$ K, $S_{\mu_f} = 111$ K, $\kappa_{0,f} = 2.41 \times 10^{-2}$, and $S_{\kappa_f} = 194$ K for air[33]. The total enthalpy and total energy which appear in the NSE are defined as follows:

$$h_t = h + \frac{1}{2}V_i V_i \tag{2.8}$$

$$e_t = h_t - \frac{p}{\rho} \tag{2.9}$$

2.1.1 Ideal Gas Law.   The NSE as represented above have six unknowns, (ρ, u, v, w, p, e_t), and 5 equations. Assuming that air is a calorically perfect gas adds the sixth equation, the ideal gas law.

$$p = \rho \mathcal{R} T \tag{2.10}$$

In the preceding equation, $\mathcal{R}$ is the universal gas constant for air.

2.1.2 Vector Form of the Navier-Stokes Equations.   The NSE can be written in conservative vector form as follows:

$$\frac{\partial U}{\partial t} + \frac{\partial \mathbf{E}}{\partial x} + \frac{\partial \mathbf{F}}{\partial y} + \frac{\partial \mathbf{G}}{\partial z} = S \tag{2.11}$$

where U is the vector of conservative variables:

$$U = \begin{bmatrix} \rho & \rho u & \rho v & \rho w & \rho e_t \end{bmatrix}^T \tag{2.12}$$

E, **F**, and **G** are the total fluxes in the x, y, and z-directions, respectively, which can be broken down into inviscid and viscous flux vectors:

$$\mathbf{E} = E_i - E_v = \begin{bmatrix} \rho u \\ \rho u^2 + p \\ \rho uv \\ \rho uw \\ \rho h_t u \end{bmatrix} - \begin{bmatrix} 0 \\ \tau_{xx} \\ \tau_{xy} \\ \tau_{xz} \\ u\tau_{xx} + v\tau_{xy} + w\tau_{xz} + q_x \end{bmatrix} \quad (2.13)$$

$$\mathbf{F} = F_i - F_v = \begin{bmatrix} \rho v \\ \rho uv \\ \rho v^2 + p \\ \rho vw \\ \rho h_t v \end{bmatrix} - \begin{bmatrix} 0 \\ \tau_{xy} \\ \tau_{yy} \\ \tau_{yz} \\ u\tau_{xy} + v\tau_{yy} + w\tau_{yz} + q_y \end{bmatrix} \quad (2.14)$$

$$\mathbf{G} = G_i - G_v = \begin{bmatrix} \rho w \\ \rho uw \\ \rho vw \\ \rho w^2 + p \\ \rho h_t w \end{bmatrix} - \begin{bmatrix} 0 \\ \tau_{xz} \\ \tau_{yz} \\ \tau_{zz} \\ u\tau_{xz} + v\tau_{yz} + w\tau_{zz} + q_z \end{bmatrix} \quad (2.15)$$

and S is the source term:

$$\mathbf{S} = \begin{bmatrix} 0 \\ 0 \\ 0 \\ 0 \\ 0 \end{bmatrix} \quad (2.16)$$

The inviscid Euler equations are formed by neglecting the viscous fluxes.

2.2 Maxwell Equations

The governing equations of electromagnetics are known as the Maxwell equations (ME). These equations are valid in all reference frames, whether observation is in the laboratory frame with the media moving relative to the observer, or the rest frame where the observer is at rest compared to the media, denoted by a prime. These equations are defined as follows and are changed to the rest frame by the addition of a prime to all terms[15]:

$$\nabla \cdot \vec{E} = \frac{\rho_e}{\epsilon_e} \tag{2.17}$$

$$\nabla \cdot \vec{B} = 0 \tag{2.18}$$

$$\nabla \times \vec{E} = -\frac{\partial \vec{B}}{\partial t} \tag{2.19}$$

$$\nabla \times \vec{B} = \mu_e \vec{j} + \mu_e \epsilon_e \frac{\partial \vec{E}}{\partial t} \tag{2.20}$$

where $\vec{E}$ is the electric field, $\vec{B}$ is the magnetic flux density, $\vec{j}$ is the conduction current density, μ_e is the permeability, and ϵ_e is the permittivity.

2.2.1 Ohm's Law. Ohm's law is defined for linear isotropic media in the rest frame as follows:

$$j_i' = \sigma_{ji} E_j' \tag{2.21}$$

where σ is the conductivity.

The Maxwell-Lorentz transformations (MLT) are used to transform the Maxwell equations from the rest frame to the laboratory frame. Several terms are added to Ohm's law during the transformation to allow for a greater range of media. When the media is nonuniform in all directions, anisotropic, and $V^2 << \mathbf{c}^2$, Ohm's law for

a nonlinear media is as follows[15]:

$$j_i = \sigma_{ji}[E_j + (\vec{V} \times \vec{B})_j] + \rho_e V_i \tag{2.22}$$

where ρ_e is the space charge.

2.2.2   Constitutive Relations.   The constitutive relations for linear isotropic dielectrics and magnetic materials expressed in the rest frame are as follows[15]:

$$\vec{E}' = \frac{\vec{D}'}{\epsilon_e} \tag{2.23}$$

$$\vec{B}' = \mu_e \vec{H}' \tag{2.24}$$

where $\vec{D}$ is the electric flux density and $\vec{H}$ is the magnetic field.

The MLT are used to transform the constitutive relations to the laboratory frame. When $V^2 << \mathbf{c}^2$ and the medium is isotropic, the constitutive relations are as follows[15]:

$$\vec{D} = \epsilon_e[\vec{E} + (1 - \frac{1}{\frac{\epsilon_e}{\epsilon_{0,e}} \frac{\mu_e}{\mu_{0,e}}})\vec{V} \times \vec{B}] \tag{2.25}$$

$$\vec{B} = \mu_e[\vec{H} - (1 - \frac{1}{\frac{\epsilon_e}{\epsilon_{0,e}} \frac{\mu_e}{\mu_{0,e}}})\vec{V} \times \vec{D}] \tag{2.26}$$

2.2.3   Magnetogasdynamic Assumptions.   When an electrically conducting fluid is moving in the presence of a magnetic field, the flow of the fluid is influenced by the field and the field is influenced by the moving fluid. If certain assumptions are made, these interactions can be expressed as equations which govern magnetofluidmechanic flow. When these assumptions are applied to a gas such as air, we apply the scientific name magnetogasdynamics and these assumptions become the MGD assumptions. The MGD assumptions are as follows[15]:

MGD Assumption 1: $|V|^2 << \mathbf{c}^2$, the magnitude of the velocities dealt with in fluid dynamics are much less than the speed of light allowing the $\sqrt{1 - (V/\mathbf{c}^2)}$ term to be set to unity.

MGD Assumption 2: $\vec{E} \approx \mathcal{O}(\vec{V} \times \vec{B})$, the electric field is of the order of any induced effects which implies that the applied magnetic field is much greater than the induced magnetic field.

MGD Assumption 3: $\frac{\partial \vec{D}}{\partial t} \approx 0$, $\frac{\partial \vec{E}}{\partial t}$ is also zero by the constitutive relations. This assumption then implies that $\nabla \times \vec{B} = \mu_e \vec{j}$.

MGD Assumption 4: $\epsilon \vec{E}^2 << \frac{\vec{B}^2}{\mu_e}$, the electric energy is insignificant compared to the magnetic energy.

MGD Assumption 5: $\vec{j} = \sigma(\vec{E} + \vec{V} \times \vec{B})$, the conductivity is also considered independent of magnetic field and constant with frequency. This assumption implies that $\vec{j}' = \vec{j}$.

MGD Assumption 6: $\vec{f} = \rho_e \vec{E} + \vec{j} \times \vec{B}$.

2.2.4   Maxwell Equations for Magnetogasdynamic Flow.   When the approximations above are applied to the ME, a new set of equations which govern electromagnetic fields are formed. These equations in the laboratory frame are as follows[15]:

$$\nabla \times \vec{E} = -\frac{\partial \vec{B}}{\partial t} \tag{2.27}$$

$$\nabla \times \vec{B} = \mu_e \vec{j} \tag{2.28}$$

$$\nabla \cdot \vec{j} = 0 \tag{2.29}$$

$$\nabla \cdot \vec{B} = 0 \tag{2.30}$$

And, Ohm's law becomes:

$$\vec{j} = \sigma(\vec{E} + \vec{V} \times \vec{B}) \tag{2.31}$$

All subsequent equations are written in the laboratory frame unless otherwise noted.

2.3   Magnetogasdynamic Equations

The Magnetogasdynamic Equations (MGDE) result from the combination of the Maxwell equations for MGD and the NSE. These equations describe the interaction between electromagnetic fields and electrically conducting gases in a continuum governed by the MGD assumptions. The MGDE are defined as follows:

$$\frac{\partial \rho}{\partial t} + \frac{\partial (\rho V_j)}{\partial x_i} = 0 \tag{2.32}$$

$$\frac{\partial (\rho V_i)}{\partial t} + \frac{\partial (\rho V_i V_j)}{\partial x_j} - \frac{\partial (p\delta_{ij})}{\partial x_j} - \frac{\partial \tau_{ij}}{\partial x_j} = \vec{j} \times \vec{B} \tag{2.33}$$

$$\frac{\partial (\rho e_t)}{\partial t} + \frac{\partial (\rho h_t V_j)}{\partial x_j} - \frac{\partial (q_j + \tau_{ji} V_i)}{\partial x_j} = \vec{E} \cdot \vec{j} \tag{2.34}$$

where $(\vec{j} \times \vec{B})$ is the Lorentz force, and $\vec{E} \cdot \vec{j}$ is the resulting energy interaction.

2.3.1   Non-dimensionalization of the Magnetogasdynamic Equations.   By non-dimensionalizing the equations, problems of different magnitude scales can be compared independent of the reference conditions. The dimensionless quantities used in the normalization of the MGDE are as follows where an asterisk represents a dimensionless quantity[15]:

$$
\begin{aligned}
L^* &= \frac{L}{L_0} & \vec{V}^* &= \frac{\vec{V}}{V_0} \\
\rho^* &= \frac{\rho}{\rho_0} & T^* &= \frac{T}{T_0} \\
\vec{E}^* &= \frac{\vec{E}}{E_0} & \vec{B}^* &= \frac{\vec{B}}{B_0}
\end{aligned}
\tag{2.35}
$$

These initial dimensional quantities of L_0, V_0, ρ_0, T_0, E_0, and B_0 are used to non-dimensionalize the other variables, and all dimensionless variables are substituted into the MGDE. Several dimensionless parameters are formed during the non-dimensionalization which help to characterize the MGD problem. The Reynolds number (Re) is the ratio of inertial forces to viscous forces, defined as follows:

$$Re = \frac{V_0 L_0}{\nu_f} \tag{2.36}$$

The magnetic Reynolds number (Rm) is a measure of the magnitude of the induced magnetic field compared to the total magnetic field:

$$Rm = V_0 L_0 \sigma_0 \mu_{0,e} \tag{2.37}$$

The Mach number (M) and magnetic Mach number (Mm) are defined as follows:

$$M = \frac{V_0}{a_0} \tag{2.38}$$

$$M_m = \frac{V_0 \sqrt{\rho_0 \mu_{0,e}}}{B_0} \tag{2.39}$$

The Prandtl number (Pr) is the ratio of kinematic viscosity to thermal diffusivity:

$$Pr = \frac{c_P \nu_f \rho_0}{\kappa_f} \tag{2.40}$$

The magnetic Prandtl number (Pm) is the ratio of vorticity diffusion to magnetic diffusion:

$$Pm = \sigma_0 \nu_f \mu_{0,e} = \frac{Rm}{Re} \tag{2.41}$$

The interaction parameter, $\mathcal{Q}$, is used when $Rm << 1$ and is defined as the ratio of the ponderomotive force to the inertial force and is $\mathcal{O}(1)$. By increasing $\mathcal{Q}$ the magnitude of the magnetic field is increased.

$$\mathcal{Q} = \frac{\sigma_0 B_0^2 L_0}{\rho_0 V_0} = \frac{Rm}{M_m^2} \tag{2.42}$$

The load factor, $\mathcal{K}$, is defined as the ratio of the electric field to the induced effects. An increase in $\mathcal{K}$ signifies a larger applied electric field, E_0.

$$\mathcal{K} = \frac{-E_0}{B_0 V_0} \tag{2.43}$$

The non-dimensional MGDE are identical to their dimensional counterparts except for the use of non-dimensional quantities and the differences in the stress tensor, heat flux, and MGD source terms.

$$\tau_{ij}^* = \frac{\mu_f^*}{Re} \left[(\frac{\partial V_i^*}{\partial x_j^*} + \frac{\partial V_j^*}{\partial x_i^*}) - \frac{2}{3} \delta_{ij} \frac{\partial V_k^*}{\partial x_k^*} \right] \tag{2.44}$$

$$q_j^* = \frac{\mu_f^*}{(\gamma - 1) M_\infty^2 RePr} \frac{\partial T^*}{\partial x_j^*} \tag{2.45}$$

The MGD source terms are now multiplied by the interaction parameter. The resulting non-dimensional Lorentz force is $\mathcal{Q}(\vec{j}^* \times \vec{B}^*)$ and the energy interaction is $\mathcal{Q}\vec{E}^* \cdot \vec{j}^*$. The non-dimensional perfect gas law is defined:

$$T^* = \frac{\gamma M_\infty^2 p^*}{\rho^*} \tag{2.46}$$

with

$$p^* = (\gamma - 1)\rho^* e^* \tag{2.47}$$

For the remainder of this document the * is dropped and all quantities are dimensionless unless otherwise noted.

2.3.2 Vector Form of the Magnetogasdynamic Equations. The equations resulting from the non-dimensionalization can then be written in a conservative vector form with the electromagnetic effects in the source term as follows:

$$\frac{\partial U}{\partial t} + \frac{\partial \mathbf{E}}{\partial x} + \frac{\partial \mathbf{F}}{\partial y} + \frac{\partial \mathbf{G}}{\partial z} = S \tag{2.48}$$

The only change from the non-dimensional conservative vector form of the NSE is in the source term S, where:

$$\mathbf{S} = \begin{bmatrix} 0 \\ \mathcal{Q}(j_y B_z - j_z B_y) \\ \mathcal{Q}(j_z B_x - j_x B_z) \\ \mathcal{Q}(j_x B_y - j_y B_x) \\ \mathcal{Q}(E_x j_x + E_y j_y + E_z j_z) \end{bmatrix} \tag{2.49}$$

2.3.3 Curvilinear Transformation. In order to accurately model most physical problems, the grid created for the physical domain has non-uniform spacing in at least one direction. This mesh might also be body-fitted involving a non-orthogonal coordinate system. To account for this, the vector form of the MGDE presented above is transformed to a generalized coordinate system (ξ,η,ζ).

$$\begin{aligned} \xi &= \xi(x, y, z) \\ \eta &= \eta(x, y, z) \\ \zeta &= \zeta(x, y, z) \\ \tau &= t \end{aligned} \tag{2.50}$$

The differential expressions for this coordinate transform are as follows:

$$
\begin{aligned}
d\xi &= \xi_x dx + \xi_y dy + \xi_z dz \\
d\eta &= \eta_x dx + \eta_y dy + \eta_z dz \\
d\zeta &= \zeta_x dx + \zeta_y dy + \zeta_z dz \\
d\tau &= dt
\end{aligned}
\tag{2.51}
$$

Similarly, the differential expressions for the inverse transformation are as follows:

$$
\begin{aligned}
dx &= x_\xi d\xi + x_\eta d\eta + x_\zeta d\zeta + x_\tau d\tau \\
dy &= y_x id\xi + y_\eta d\eta + y_\zeta d\zeta + y_\tau d\tau \\
dz &= z_x id\xi + z_\eta d\eta + z_\zeta d\zeta + z_\tau d\tau \\
dt &= d\tau
\end{aligned}
\tag{2.52}
$$

The transformation metrics are defined using Equation 2.51 and Equation 2.52[31]:

$$
\begin{aligned}
\xi_x &= J(y_\eta z_\zeta - y_\zeta z_\eta) \\
\xi_y &= -J(x_\eta z_\zeta - x_\zeta z_\eta) \\
\xi_x &= J(y_\eta y_\zeta - y_\zeta y_\eta)
\end{aligned}
\tag{2.53}
$$

$$
\begin{aligned}
\eta_x &= -J(y_\xi z_\zeta - y_\zeta z_\xi) \\
\eta_y &= J(x_\xi z_\zeta - x_\zeta z_\xi) \\
\eta_x &= -J(y_\xi y_\zeta - y_\zeta y_\xi)
\end{aligned}
\tag{2.54}
$$

2-11

$$\zeta_x = J(y_\xi z_\eta - y_\eta z_\xi)$$

$$\zeta_y = -J(x_\xi z_\eta - x_\eta z_\xi) \qquad (2.55)$$

$$\zeta_x = J(y_\xi y_\eta - y_\eta y_\xi)$$

where the Jacobian of transformation, J, is defined as follows[31]:

$$J = \frac{1}{x_\xi(y_\eta z_\zeta - y_\zeta z_\eta) - x_\eta(y_\xi z_\zeta - y_\zeta z_\xi) + x_\zeta(y_\xi z_\eta - y_\eta z_\xi)} \qquad (2.56)$$

Applying the transformations to Equation 2.48 and manipulating the equation into strong conservation form, the new terms $\hat{U}$, $\hat{E}$, $\hat{F}$, $\hat{G}$, and $\hat{S}$ are formed.

$$\hat{U} = \frac{U}{J}$$

$$\hat{\mathbf{E}} = \frac{1}{J}(\mathbf{E}\xi_x + \mathbf{F}\xi_y + \mathbf{G}\xi_z)$$

$$\hat{\mathbf{F}} = \frac{1}{J}(\mathbf{E}\eta_x + \mathbf{F}\eta_y + \mathbf{G}\eta_z) \qquad (2.57)$$

$$\hat{\mathbf{G}} = \frac{1}{J}(\mathbf{E}\zeta_x + \mathbf{F}\zeta_y + \mathbf{G}\zeta_z)$$

$$\hat{S} = \frac{S}{J}$$

with the resulting vector equation[31]:

$$\frac{\partial \hat{U}}{\partial \tau} + \frac{\partial \hat{\mathbf{E}}}{\partial \xi} + \frac{\partial \hat{\mathbf{F}}}{\partial \eta} + \frac{\partial \hat{\mathbf{G}}}{\partial \zeta} = \hat{S} \qquad (2.58)$$

3. Numerical Implementation

This section presents the discretization of the Magnetogasdynamic Equations as they are employed in the AFRL/VAAC three-dimensional MGD CFD code[3, 4, 5, 6, 7, 8]. For this inviscid research study, the viscous terms in the MGDE are neglected. The curvilinear vector form of the MGDE, Eqn. 2.58, on page 2-12 is rewritten as follows:

$$\frac{\partial \hat{U}}{\partial \tau} + \frac{\partial \hat{E}}{\partial \xi} + \frac{\partial \hat{F}}{\partial \eta} + \frac{\partial \hat{G}}{\partial \zeta} = \hat{S} \tag{3.1}$$

where the fluxes are inviscid

$$\begin{aligned}
\hat{E} &= \frac{1}{J}(E_I \xi_x + F_I \xi_y + G_I \xi_z) \\
\hat{F} &= \frac{1}{J}(E_I \eta_x + F_I \eta_y + G_I \eta_z) \\
\hat{G} &= \frac{1}{J}(E_I \zeta_x + F_I \zeta_y + G_I \zeta_z)
\end{aligned} \tag{3.2}$$

Equation 3.1 is solved using a nodal finite-volume approach. The physical grid is transformed to the evenly spaced computational grid using Eqns. 2.53, 2.54, and 2.55. The discretization of Equation 3.1 has the form:

$$\frac{\partial \hat{U}}{\partial \tau} = -\mathbf{R}(\hat{U})^n_{i,j,k} \tag{3.3}$$

where $\mathbf{R}$ is the residual vector:

$$\begin{aligned}
\mathbf{R}(\hat{U})^n_{i,j,k} = \hat{E}^n_{i+1/2,j,k} - \hat{E}^n_{i-1/2,j,k} + \hat{F}^n_{i,j+1/2,k} - \hat{F}^n_{i,j-1/2,k} \\
+ \hat{G}^n_{i,j,k+1/2} - \hat{G}^n_{i,j,k-1/2} + \hat{S}^n_{i,j,k}
\end{aligned} \tag{3.4}$$

The indices (i, j, k) represent the node values, and the indices $(i \pm 1/2, j, k)$, $(i, j \pm 1/2, k)$, and $(i, j, k \pm 1/2)$ represent the right/left, top/bottom, and front/back cell interfaces, respectively.

3.1 Flux Representation

The fluxes across the boundaries of each cell, $\hat{E}$, $\hat{F}$, and $\hat{G}$, are defined as follows[31]:

$$\hat{E} = \frac{1}{J} \begin{bmatrix} \rho \mathcal{U} \\ \rho u \mathcal{U} + \xi_x p \\ \rho v \mathcal{U} + \xi_y p \\ \rho w \mathcal{U} + \xi_z p \\ \rho h_t \mathcal{U} \end{bmatrix} \tag{3.5}$$

$$\hat{F} = \frac{1}{J} \begin{bmatrix} \rho \mathcal{V} \\ \rho u \mathcal{V} + \eta_x p \\ \rho v \mathcal{V} + \eta_y p \\ \rho w \mathcal{V} + \eta_z p \\ \rho h_t \mathcal{V} \end{bmatrix} \tag{3.6}$$

$$\hat{G} = \frac{1}{J} \begin{bmatrix} \rho \mathcal{W} \\ \rho u \mathcal{W} + \zeta_x p \\ \rho v \mathcal{W} + \zeta_y p \\ \rho w \mathcal{W} + \zeta_z p \\ \rho h_t \mathcal{W} \end{bmatrix} \tag{3.7}$$

where $\mathcal{U}$, $\mathcal{V}$, and $\mathcal{W}$ are the contravariant velocity components in the ξ, η, and ζ directions, respectively, defined as follows:

$$
\begin{aligned}
\mathcal{U} &= \xi_x u + \xi_y v + \xi_z w & (3.8) \\
\mathcal{V} &= \eta_x u + \eta_y v + \eta_z w & \\
\mathcal{W} &= \zeta_x u + \zeta_y v + \zeta_z w & (3.9)
\end{aligned}
$$

3.1.1 Roe Flux-Difference Splitting Scheme. The flux vectors are discretized using Roe's upwind method with a van Leer harmonic limited Monotone Upstream-centered Schemes for Conservation Laws (MUSCL) variable extrapolation[28, 32, 11]. The Roe scheme is a flux-difference splitting method created to more accurately capture the discontinuities present in high-speed fluids. Roe's algorithm is applied to each coordinate independently. The following derivation applies the Roe scheme in the ξ direction. The cell interface flux is written as the exact solution to an approximate Riemann problem[32], given by

$$
\hat{E}_{i+1/2,j,k} = \frac{1}{2} \left[\hat{E}(U_L) + \hat{E}(U_R) - |\tilde{\mathbf{A}}|(U_R - U_L) \right]_{i+1/2,j,k} \tag{3.10}
$$

where $\tilde{\mathbf{A}}$ is the flux jacobian

$$
\tilde{\mathbf{A}} = \frac{\partial \hat{E}}{\partial U} \tag{3.11}
$$

The Roe vector in Eqn. 3.10 can now be defined as follows[32]:

$$
|\tilde{\mathbf{A}}|(U_R - U_L) = |\tilde{\mathbf{A}}|\Delta U = \begin{bmatrix} \alpha_4 \\ \tilde{u}\alpha_4 + k_x\alpha_5 + \alpha_6 \\ \tilde{v}\alpha_4 + k_y\alpha_5 + \alpha_7 \\ \tilde{W}\alpha_4 + k_z\alpha_5 + \alpha_8 \\ \tilde{H}\alpha_4 + \tilde{\tilde{u}}\alpha_5 + \tilde{u}\alpha_6 + \tilde{v}\alpha_7 + \tilde{w}\alpha_8 - \dfrac{\tilde{a}^2}{\gamma - 1}\alpha_1 \end{bmatrix} \tag{3.12}
$$

3-3

where the α terms are defined

$$\alpha_1 = \left|\frac{\nabla\xi}{J}\right| |\tilde{\tilde{u}}| \left(\Delta\rho - \frac{\Delta p}{\tilde{a}^2}\right)$$

$$\alpha_2 = \frac{1}{2\tilde{a}^2} \left|\frac{\nabla\xi}{J}\right| |\tilde{\tilde{u}} + \tilde{a}|(\Delta p + \tilde{\rho}\tilde{a}\Delta\bar{u})$$

$$\alpha_3 = \frac{1}{2\tilde{a}^2} \left|\frac{\nabla\xi}{J}\right| |\tilde{\tilde{u}} - \tilde{a}|(\Delta p - \tilde{\rho}\tilde{a}\Delta\bar{u})$$

$$\alpha_4 = \alpha_1 + \alpha_2 + \alpha_3 \qquad\qquad (3.13)$$

$$\alpha_5 = \tilde{a}(\alpha_2 - \alpha_3)$$

$$\alpha_6 = \left|\frac{\nabla\xi}{J}\right| |\tilde{\tilde{u}}| \left(|r\tilde{h}o\Delta u - k_x r\tilde{h}o\Delta\bar{u}\right)$$

$$\alpha_7 = \left|\frac{\nabla\xi}{J}\right| |\tilde{\tilde{u}}| \left(|r\tilde{h}o\Delta v - k_y r\tilde{h}o\Delta\bar{u}\right)$$

$$\alpha_8 = \left|\frac{\nabla\xi}{J}\right| |\tilde{\tilde{u}}| \left(|r\tilde{h}o\Delta w - k_z r\tilde{h}o\Delta\bar{u}\right)$$

The interface areas and normal velocity terms are defined as follows:

$$k_x = \frac{\xi_x}{|\nabla\xi|}$$

$$k_y = \frac{\xi_y}{|\nabla\xi|} \qquad\qquad (3.14)$$

$$k_z = \frac{\xi_z}{|\nabla\xi|}$$

$$\bar{u} = k_x u + k_y v + k_z w$$

In the above equations, the Roe averaged variables are defined as follows:

$$
\begin{aligned}
R_{i+1/2} &= \sqrt{\frac{\rho_R}{\rho_L}} \\
\tilde{\rho}_{i+1/2} &= \rho_L R_{i+1/2} \\
\tilde{u}_{i+1/2} &= \frac{u_L + u_R R_{i+1/2}}{1 + R_{i+1/2}} \\
\tilde{\bar{u}}_{i+1/2} &= \frac{\bar{u}_L + \bar{u}_R R_{i+1/2}}{1 + R_{i+1/2}} \\
\tilde{v}_{i+1/2} &= \frac{v_L + v_R R_{i+1/2}}{1 + R_{i+1/2}} \\
\tilde{w}_{i+1/2} &= \frac{w_L + w_R R_{i+1/2}}{1 + R_{i+1/2}} \\
\tilde{H}_{i+1/2} &= \frac{H_L + H_R R_{i+1/2}}{1 + R_{i+1/2}} \\
\tilde{a}^2_{i+1/2} &= (\gamma - 1)[\tilde{H}_{i+1/2} - (\tilde{u}^2 + \tilde{v}^2 + \tilde{w}^2)/2]
\end{aligned}
\tag{3.15}
$$

The Roe scheme is capable of producing a non-physical expansion shock given certain conditions. The expansion shock violates the second law of thermodynamics. In order to prevent this occurrence, an entropy fix is added to the Roe scheme[31]. For the problem examined in the current research, the conditions needed to form an expansion shock are not present.

3.1.2 MUSCL Higher-Order Variable Extrapolation. In order to achieve a higher order of spatial accuracy, the primitive variable vector to the left and right of the cell interface is extrapolated. The primitive variable vector, $\mathbf{V}$, is defined

$$
\mathbf{V} = \begin{bmatrix} \rho \\ u \\ v \\ w \\ p \end{bmatrix}
\tag{3.16}
$$

3-5

The higher order left and right cell interface values of the primitive variables are calculated using a van Leer harmonic limited MUSCL variable extrapolation[11]. The limiter prevents the slope across the interface from exceeding stability bounds.

$$(\mathbf{V}_L)_{i+1/2} = \mathbf{V}_i + \frac{1}{4}[(1-\kappa_l)\Phi^+_{i-1/2}(\mathbf{V}_i - \mathbf{V}_{i-1})+$$
$$(1+\kappa_l)\Phi^-_{i+1/2}(\mathbf{V}_{i+1} - \mathbf{V}_i)] \quad (3.17)$$

$$(\mathbf{V}_R)_{i+1/2} = \mathbf{V}_{i+1} + \frac{1}{4}[(1-\kappa_l)\Phi^-_{i+3/2}(\mathbf{V}_{i+2} - \mathbf{V}_{i+1})+$$
$$(1+\kappa_l)\Phi^+_{i+1/2}(\mathbf{V}_{i+1} - \mathbf{V}_i)] \quad (3.18)$$

where

$$
\begin{aligned}
\Phi^-_{i+1/2} &= \frac{r^-_{1+1/2} + |r^-_{1+1/2}|}{1 + r^-_{1+1/2}} \\
\Phi^-_{i+3/2} &= \frac{r^-_{1+3/2} + |r^-_{1+3/2}|}{1 + r^-_{1+3/2}} \\
\Phi^+_{i-1/2} &= \frac{r^+_{1-1/2} + |r^+_{1-1/2}|}{1 + r^+_{1-1/2}} \\
\Phi^+_{i+1/2} &= \frac{r^+_{1+1/2} + |r^+_{1+1/2}|}{1 + r^+_{1+1/2}}
\end{aligned}
\quad (3.19)
$$

and

$$
\begin{aligned}
r^-_{i+1/2} &= \frac{\mathbf{V}_i - \mathbf{V}_{i-1}}{\mathbf{V}_{i+1} - \mathbf{V}_i} \\
r^-_{i+3/2} &= \frac{\mathbf{V}_{i+1} - \mathbf{V}_i}{\mathbf{V}_{i+2} - \mathbf{V}_{i+1}} \\
r^+_{i-1/2} &= \frac{\mathbf{V}_{i+1} - \mathbf{V}_i}{\mathbf{V}_i - \mathbf{V}_{i-1}} \\
r^+_{i+1/2} &= \frac{\mathbf{V}_{i+2} - \mathbf{V}_{i+1}}{\mathbf{V}_{i+1} - \mathbf{V}_i}
\end{aligned}
\quad (3.20)
$$

3-6

In Eqns. 3.17 and 3.18, κ_l is set to 1/3 for the higher-order calculations and the left and right cell interface values are set to the i and $i + 1$ node values, respectively, for first-order calculations.

3.2 Temporal Discretization

The code includes an explicit Runge-Kutta time integration method and an implicit Beam-Warming time integration method. Explicit schemes severely limit the time step-size based on the size of the cells in the physical domain. These limitations are made worse near the wall where the mesh is very fine and there are large stretch factors[6]. To avoid this, an implicit method with a sub-iteration strategy is incorporated to solve the low magnetic Reynolds number form of the governing equations. This integration is covered in detail by Gaitonde and Poggie in Ref. [6], including validation of the implicit scheme. The basic formula to compute the change in the solution vector, ΔU, is:

$$
\begin{aligned}
\left[J^{-1} + \frac{1}{1+\phi}\Delta\tau \ \ \delta_\xi \hat{\mathbf{A}}^{\mathbf{p}} \right] J \cdot \left[J^{-1} + \frac{1}{1+\phi}\Delta\tau \ \ \delta_\eta \hat{\mathbf{B}}^{\mathbf{p}} \right] & \\
J \cdot \left[J^{-1} + \frac{1}{1+\phi}\Delta\tau \ \ \delta_\zeta \hat{\mathbf{C}}^{\mathbf{p}} \right] \Delta U &= \\
-\frac{1}{1+\phi}\Delta\tau \left[J^{-1}\frac{(1+\phi)X^p - (1+2\phi)X^n + \phi X^{n-1}}{\Delta\tau} + \hat{\mathbf{R}}^{\mathbf{p}} \right]
\end{aligned}
\tag{3.21}
$$

In Eqn. 3.21 $\Delta\tau$ is the generalized time-step size, δ_ξ, δ_η, and δ_ζ denote central second-order difference operators and ϕ controls the temporal order of accuracy of the scheme. $\hat{\mathbf{A}}$, $\hat{\mathbf{B}}$ and $\hat{\mathbf{C}}$ are transformed flux Jacobians and $\hat{R}$ is the residual evaluated with the Roe scheme.

Sub-iterations, indicated by the counter p in Eqn. 3.21, reduce linearization, factorization, and explicit boundary condition implementation errors. Each iteration typically requires two or three sub-iterations to achieve inner-iteration convergence[6].

3.3 Computational Set-up

Figure 3.1 illustrates the physical domain used for this work. Increases in θ were accomplished by moving the leading edge of the ramp down and back, effectively opening up the inlet. The ratio g/w was held constant at 0.34 by allowing the ramp to be hinged at the throat. Fine 213×99 grids were created for all compression angles, $22^o \leq \theta \leq 28^o$.
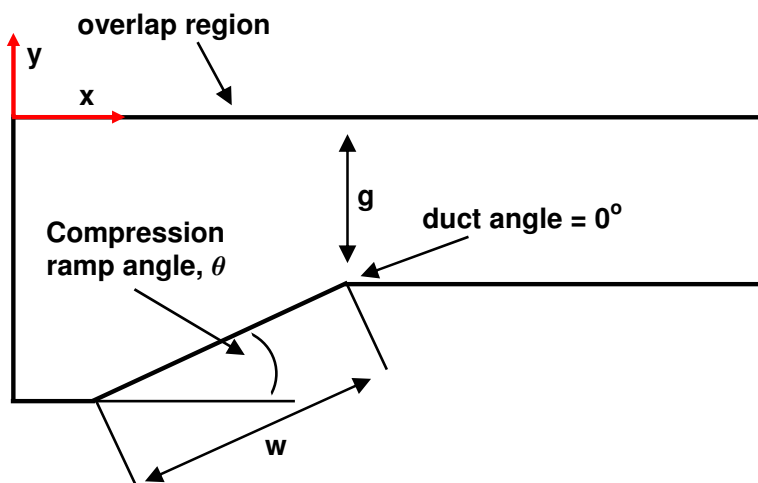
Figure 3.1   Schematic of the two-dimensional domain

The duct angle in Fig. 3.1 is 0°. This difference from Schmisseur and Gaitonde's domain[30] shown in Fig. 1.9 is due to inaccuracies encountered with a duct angle of 25.4^o. The expansion angle created by combining θ and the duct angle of 25.4^o was too large for inviscid flow. This expansion angle caused the computational code using Roe flux-differencing to become unstable. The early work with the 25.4^o duct angle used the finite-compact-differencing scheme with dampening presented by Gaitonde in Ref. [3]. This numerical scheme introduced artificial viscosity for dampening, allowing the inviscid flowfield to converge inaccurately. Discovery of this problem led to the 0° duct angle shown in Fig. 3.1.

The computations for this inviscid study were performed at a Mach number of 4.96. In order to completely determine the freestream variables, the Reynolds number based on w was set to 2 million. A coarse, fine, and ultra-fine mesh were

created for the $\theta = 26^o$ ramp angle. These grids were used for the mesh refinement study. Figure 3.2 shows the coarse, fine, and ultra-fine 26° mesh. The line running near the top of the domain is the symmetry plane. The coarse grid is 107×50, and the ultra-fine grid is 425×197. Each grid refinement step-up corresponds to exactly twice the cells in both the ξ and η directions. All grids include a mirror image of the top four rows about $y = 0$. These extra rows are used for a symmetry boundary condition. The computations included 5 total planes in ζ direction. The two planes on each side of the center plane are copies of the center plane forcing the solutions to be two-dimensional.

The magnetogasdynamic equations resolve the flow within the domain, but boundary conditions must be specified to define the flow conditions along the computational boundary. The MGD code reverts to first order at the boundaries. This facilitates solution of a domain without resorting to non-physical "ghost" nodes to create higher-order boundary conditions.

For the current research, the entrance of the inlet is an inflow condition and the exit is an outflow condition. The walls of the inlet are specified as an inviscid-slip boundary condition and the inlet is symmetric, so only half the inlet is modelled to decrease the number of nodes and corresponding computational time. A symmetry boundary condition (BC) is applied along the split.

The hypersonic flow conditions allow the use of a supersonic inflow BC on the entrance to the inlet. The values of the primitive variables on the boundary, $\mathbf{V}_{(1,j,k)}$, are equal to the freestream values of ρ, u, v, w, and p. With the non-dimensionalization, $\rho = u = 1$, $v = w = 0$, and $p = p_0/(\rho_0 u_0^2)$. Figure 3.3 illustrates the supersonic inflow BC.

The flow exiting the inlet should remain supersonic due to the expansion after the compression ramp. This allows specification of a supersonic outflow BC at the exit of the inlet. The values of the primitive variables on the boundary, $\mathbf{V}_{(ni,j,k)}$, are equal to the primitive variable values one node in, $\mathbf{V}_{(ni-1,j,k)}$, as shown in Fig. 3.3.
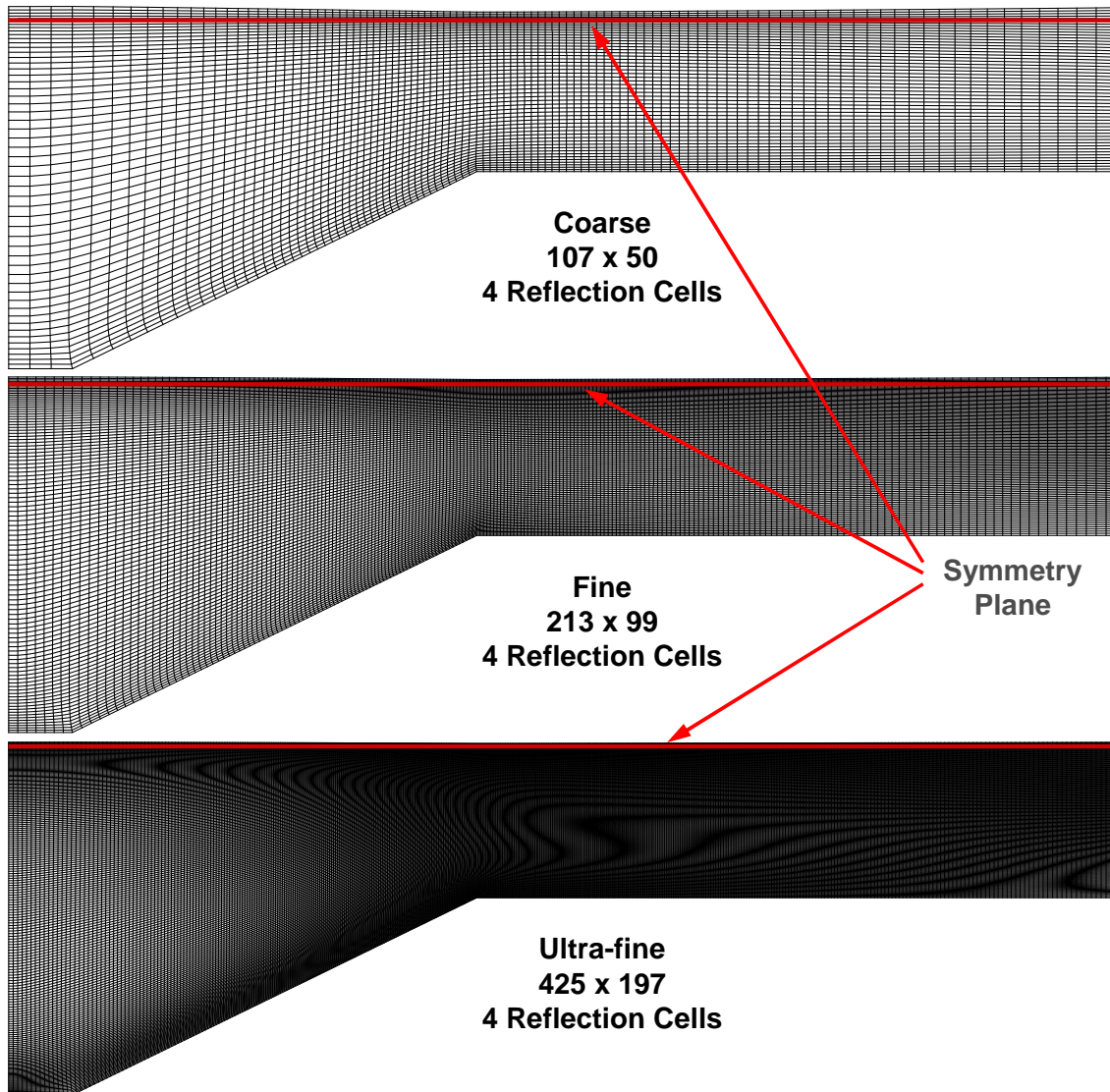
Figure 3.2   26º coarse, fine, and ultra-fine grids with corresponding symmetry line, $g/w = 0.34$
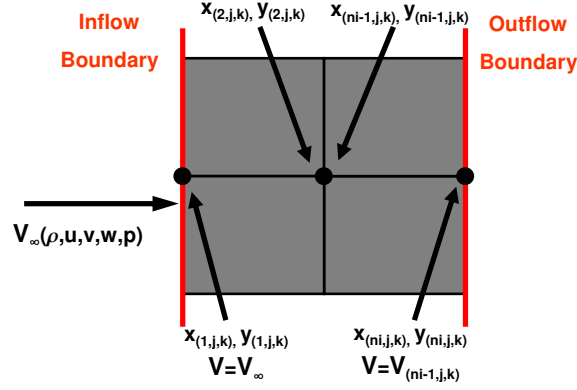
Figure 3.3   Schematic of the supersonic inflow and outflow BCs

The values are simply copied from the $(ni-1, j, k)$ location to the boundary location at (ni, j, k).

The symmetry boundary condition simply specifies that the nodes above the symmetry plane are mirrored from the nodes below the plane. If the symmetry plane falls at (i, nj, k), the primitive variables one node above, $\mathbf{V}_{(i,nj+1,k)}$, are set to the values one node below, $\mathbf{V}_{(i,nj-1,k)}$. The trend, $\mathbf{V}_{(i,nj+m,k)} = \mathbf{V}_{(i,nj-m,k)}$, continues incrementing until $m = 4$. The symmetry BC at the center of the inlet decreases the number of nodes by almost 50%, correspondingly decreasing the computation time for convergence.

The inviscid slip BC along the surface of the inlet projects the velocity vector one node from the wall, $U_{(i,2,k)}$ onto the surface of the wall, as shown in Fig. 3.4. The velocity in the z-direction, w, is set to zero. This process starts with calculation of the angle of the wall, Θ_B, as follows

$$\Theta_B = \arctan\left(\frac{y_{(i-1,1,k)} - y_{(i,1,k)}}{x_{(i-1,1,k)} - x_{(i,1,k)}}\right) \tag{3.22}$$

The velocity vector, $U_{(i,2,k)}$ at one node in is then projected onto the wall. The magnitude of this velocity is calculated as follows

$$||U_{(i,1,k)}|| = \cos(\Theta_B)u_{(i,2,k)} + \sin(\Theta_B)v_{(i,2,k)} \tag{3.23}$$

3-11

The u and v components of $U_{(i,1,k)}$ shown in Fig. 3.4 are then calculated

$$u_{(i,1,k)} = \cos(\Theta_B)||U_{(i,1,k)}|| \qquad (3.24)$$

$$v_{(i,1,k)} = \sin(\Theta_B)||U_{(i,1,k)}||$$
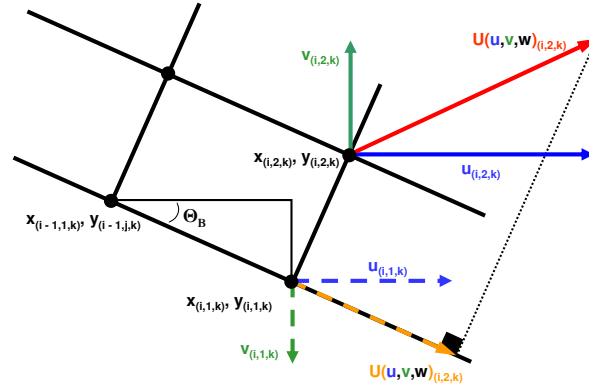
Figure 3.4   Schematic of the inviscid slip BCs

The pressure and density at the specified wall location are set equal to the pressure and density one node in, $p_{(i,1,k)} = p_{(i,2,k)}$ and $\rho_{(i,1,k)} = \rho_{(i,2,k)}$.

For all compression angles $\theta < 28^o$, the regular symmetry solutions were obtained by first initializing the domain to the freestream. Next, the flowfield was iterated until the RR solution converged. Compression angles greater than or equal to 28° would not resolve a RR, converging instead to a MR.

Mach reflection solutions for $\theta < 28^o$ were obtained from a 28° MR solution. The 28° MR solution was used as the initial condition for the 27° MR solution. Once the 27° MR had converged, the resulting MR solution was used as the starting point for obtaining the 26° MR. Each lower θ used the same procedure initializing the domain to the converged MR solution of the next higher θ.

Accelerating and decelerating Lorentz forces are applied to the converged MR and RR solutions, respectively, as shown in Figures 3.5 and 3.6. The applied non-

dimensional magnetic field is given a magnitude of 1 since the magnetic flux density, $\vec{B}$, is non-dimensionalized by B_0. The magnetic field for the accelerating Lorentz force is shown in Fig. 3.6 with $\vec{B}$ in the $-y$ direction. For the decelerating force, the magnetic field is aligned with $+y$ direction as shown in Fig. 3.5. Both accelerating and decelerating forces require the electric field applied in the positive z-direction with E_0 nominally set to 1.2.
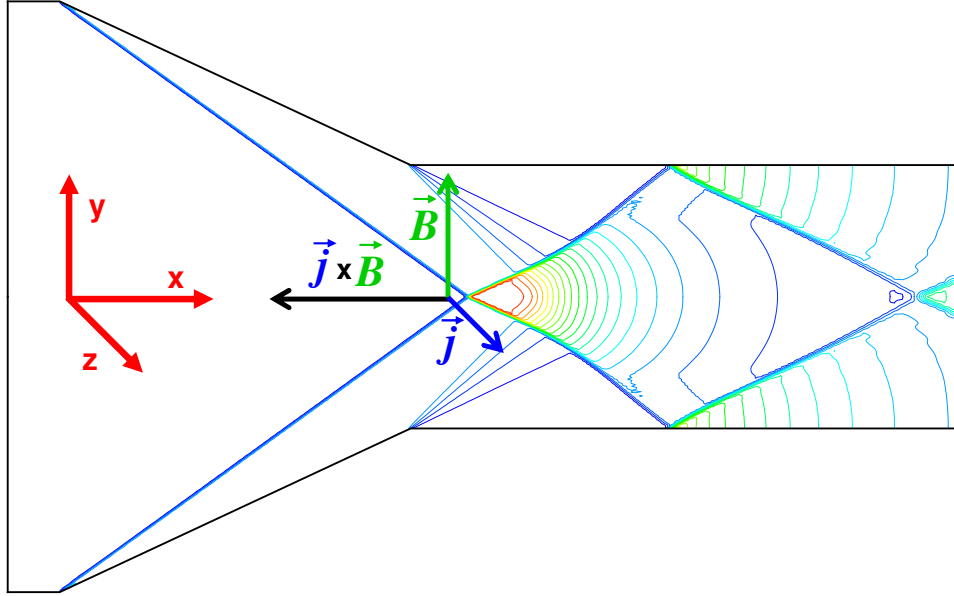
Figure 3.5   Schematic of the decelerating Lorentz force on the $25^o \times 25^o$ Regular Reflection

The Lorentz force is applied in a select area defined by the conductivity tensor as shown in Fig. 3.7. The electrical conductivity tensor, $\bar{\bar{\sigma}}$, is calculated as products of modified Gaussians of the form[4]:

$$\sigma_1 = Ae^{-a(s-s_0)^n} \tag{3.25}$$

where A is set to unity, n is set to 6, a is the half-width, δ_x or δ_y, s_0 is the center of conductivity, x_0 or y_0, and $s - s_0$ represents the distance from center of conductivity, illustrated in Fig. 3.7. Beyond the region defined by $x_0 \pm \delta_x$ and $y_0 \pm \delta_y$ the conduc-
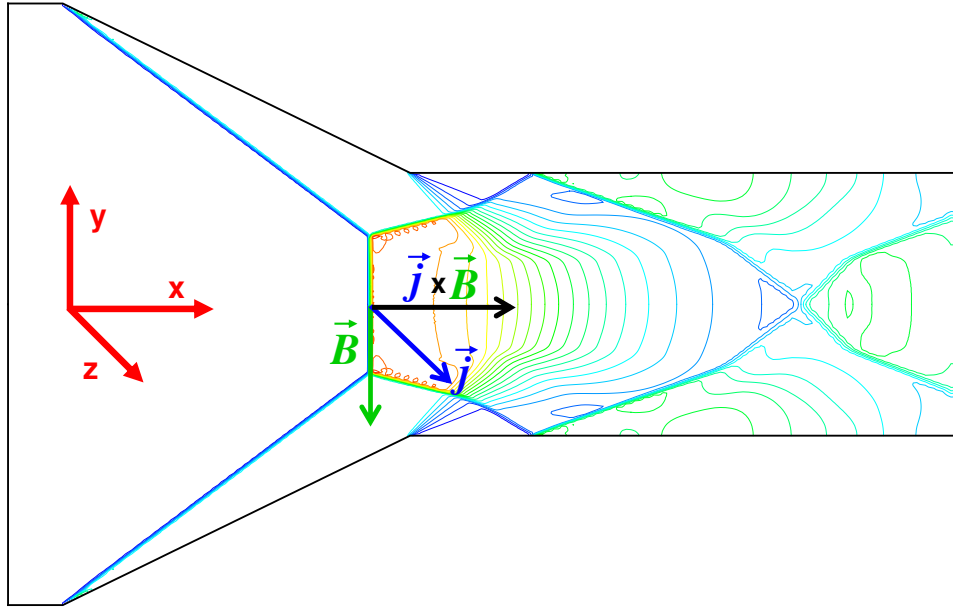
Figure 3.6   Schematic of the accelerating Lorentz force on the $26^o \times 26^o$ Mach Reflection

tivity is zero. This specification drives the electrical current, j, to zero by Eqn. 2.31, subsequently setting all electromagnetic effects to zero.

The various conductivity specifications are shown in Table 3.1. All computations centered the applied force on the centerline of the inlet, $y_0 = 0.0$. Figure 3.8 shows the six cases with $x_0 = 0.8175$, which places the center of conductivity coincident with the 26° Mach reflection. The conductivity was varied lengthwise and across the width including Case 2.4.4 with constant σ.

Figure 3.9 shows the two cases with $x_0 = 0.4$. At this location, the applied MGD force remains entirely in front of the 26° MR. This accelerates the flow prior to the shocks, with either a small region of force in the center, Case 1.1.1, or a force that gradually tapers away from the center, Case 1.2.1.

Figure 3.10 shows the two cases with $x_0 = 1.6$. The conductivity is specified to remain entirely behind a Mach or regular reflection. The flow behind the shock formation is accelerated by the small region of force in the center, Case 3.1.1, or the force that gradually tapers away from the center, Case 3.2.1.
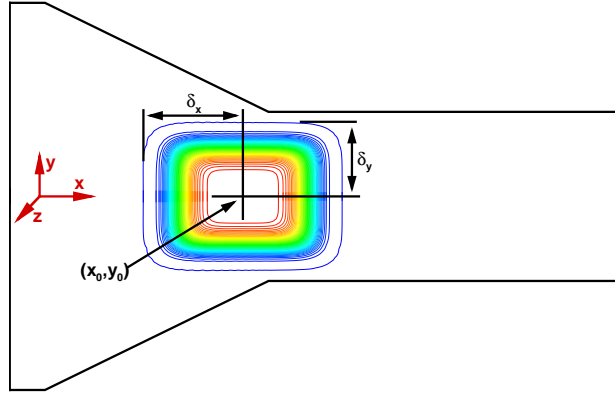
Figure 3.7   Area of applied Lorentz force defined by Equation 3.25

Table 3.1   Specified conductivity, σ, parameters

Conductivity Settings	Case #	x_0	y_0	δ_x	δ_y
Front Location, Center Focus	Case 1.1.1	0.4	0.0	0.4	0.3
Front Location, Gradient Width	Case 1.2.1	0.4	0.0	0.4	0.7
MR Location, Center Focus	Case 2.1.1	0.8175	0.0	0.4	0.3
MR Location, Gradient Width	Case 2.2.1	0.8175	0.0	0.4	0.7
MR Location, Gradient Full	Case 2.2.2	0.8175	0.0	1.5	0.7
MR Location, Full Width	Case 2.3.1	0.8175	0.0	50	50
MR Location, Full Width, Half Length	Case 2.3.3	0.8175	0.0	0.2	50
MR Location, Constant σ	Case 2.4.4	0.8175	0.0	50	50
Rear Location, Center Focus	Case 3.1.1	1.6	0.0	0.4	0.3
Rear Location, Gradient Width	Case 3.2.1	1.6	0.0	0.4	0.7

MR Location, Center Focus
2.1.1

MR Location, Gradient Width
2.2.1

MR Location, Gradient Full
2.2.2

MR Location, Full Width
2.3.1

MR Location, Full Width, Half Length
2.3.3

MR Location, Constant σ
2.4.4
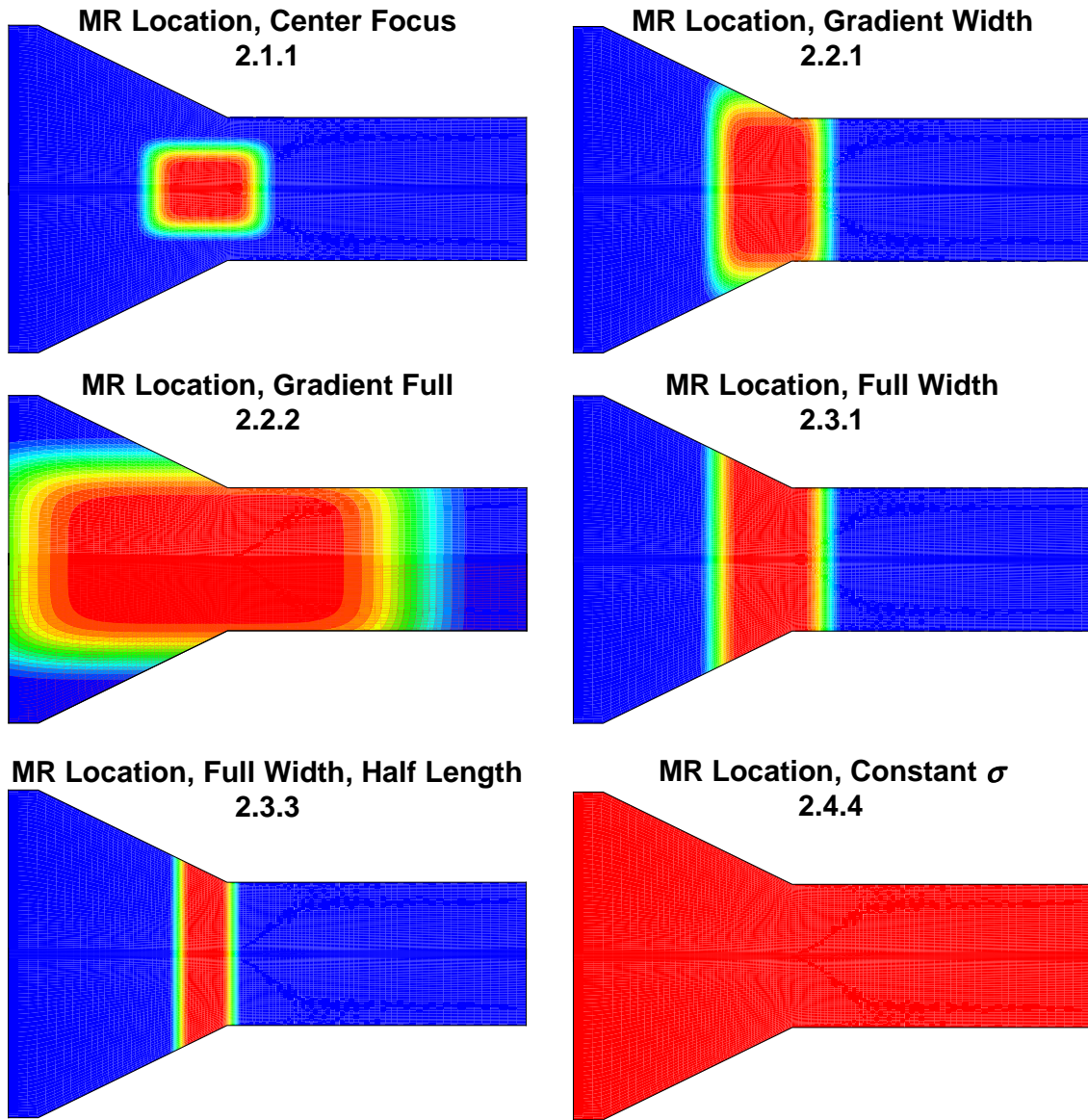
Figure 3.8   Conductivity centered at the 26° MR, Cases 2.1.1, 2.2.1 , 2.2.2, 2.3.1,
2.3.3, 2.4.4

**Front Location, Center Focus
1.1.1**

**Front Location, Gradient Width
1.2.1**
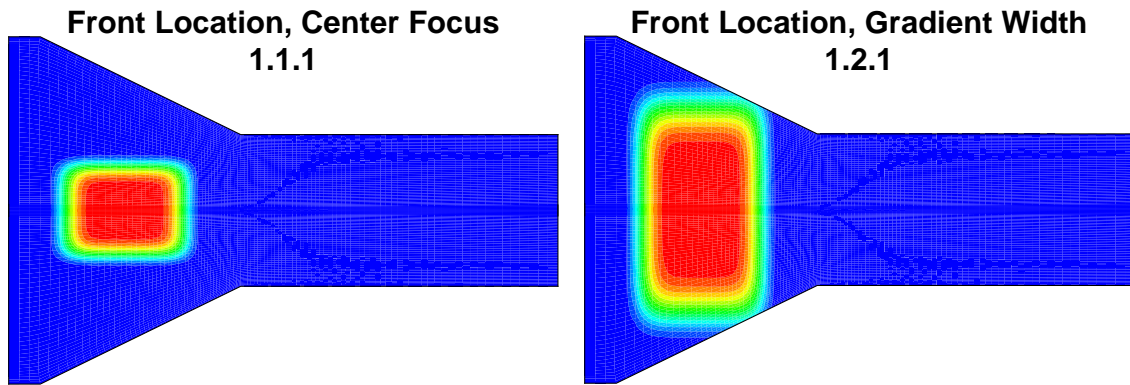
Figure 3.9   Conductivity centered in front of the 26° MR, Cases 1.1.1, 1.2.1

**Rear Location, Center Focus
3.1.1**

**Rear Location, Gradient Width
3.2.1**
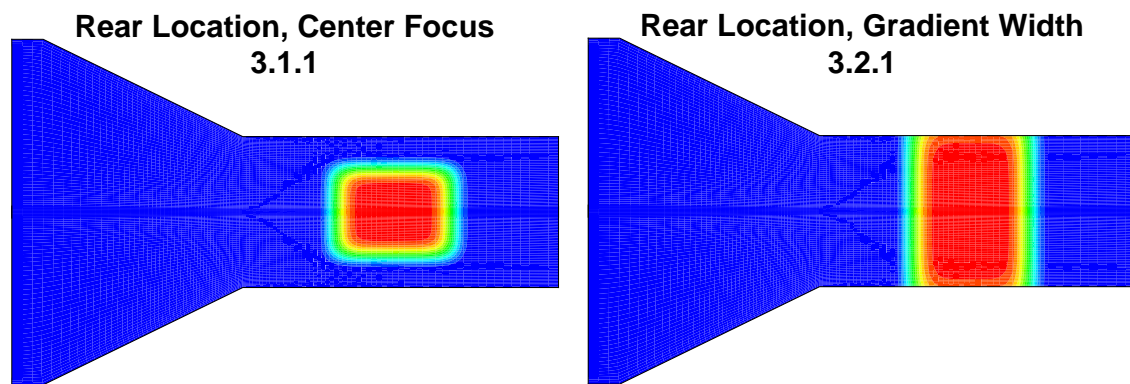
Figure 3.10   Conductivity centered behind the 26° MR and the moved MR, Cases
3.1.1, 3.2.1

4. Results

The regular and Mach reflection solutions for compression angles of 25° and 26° in the dual-solution domain were used in this numerical study to investigate the effect magnetogasdynamics has on these shock structures. Figures 1.5 and 1.6 show the 25° RR and MR numerical solutions, respectively. Figure 4.1 shows the 26° dual-solution domain with the RR presented on bottom and the MR on top. For this numerical study, the 25° RR was subjected to a decelerating Lorentz force in order to determine the sensitivity of transitioning a RR to an undesired MR. The 26° MR was subjected to an accelerating Lorentz force to determine its capability of transitioning a MR to a desired RR and suppressing inlet unstart.
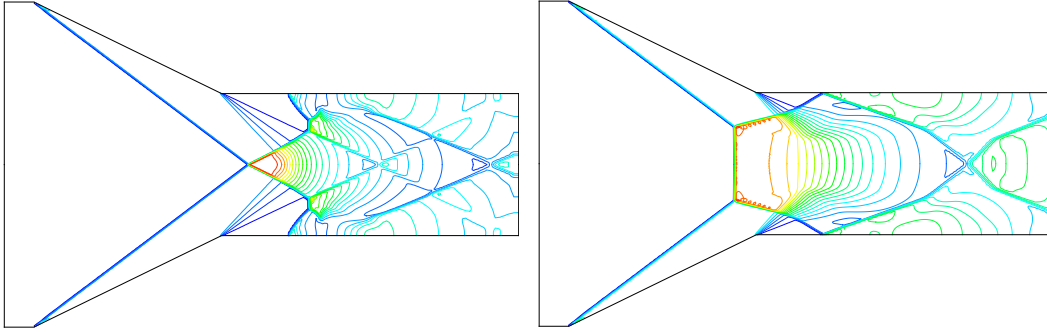
Figure 4.1   Pressure contours from a regular and Mach reflection for Mach 4.96, 2-D solutions, $26^o \times 26^o$ (MR-right, RR-left)

The MGD code uses temperature, Mach number, and Reynolds number to calculate the flow variables for each solution. The current research used freestream flow parameters of $Re = 2 \times 10^6$ (based on $w = 1\ m$), $M_0 = 4.96$, $T_0 = 72.54\ K$, $\rho_0 = 1.1614 \times 10^{-2}\ kg/m^3$, $p_0 = 241.776\ Pa$, $V_0 = 846.76\ m/s$, and $t_0 = 1.118 \times 10^{-3}\ s$ were employed in this research. The corresponding total pressure and total temperature were $1.22 \times 10^5\ Pa$ and $429.43\ K$, respectively. These parameters were chosen to match the experimental work of Ivanov, et al. and the numerical work of Schmisseur and Gaitonde[17, 20, 29, 30].

The magnetogasdynamic effects were applied to the flowfield using a magnetic flux density set to a nominal value of $B_0 = 2.0\ T$ for $\mathcal{Q} = 1$. The resulting maximum magnitude of the conductivity, σ_0, was 2.459 mho/m based on Eqn. 2.42. The magnitude of the applied electric field, E_0, is 2032.23 v/m from Eqn. 2.43. These values resulted in a magnetic Reynolds number, $Rm = 0.0026$ (Eqn. 2.37), much less than 1 as required for the source term formulation of the MGDE. When the interaction parameter was increased, the magnitude of the conductivity was kept constant and the magnetic field was increased as required. For this research, $\mathcal{Q} = 10.0$ was the largest interaction parameter investigated, which equates to a required magnetic flux density magnitude of 6.325 T and a maximum applied electric field of 6426.49 v/m.

4.1 Hysteresis

Schmisseur and Gaitonde's hysteresis for $g/w = 0.34$ (Fig. 1.10)[30] is duplicated in Fig. 4.2. The shock structure remains in a RR configuration until $\theta > 27^o$. After transitioning to a MR configuration, the Mach reflection remains until $\theta \leq 22^o$. This hysteresis matches Schmisseur and Gaitonde's numerical results[30], the initial point for the magnetogasdynamic study in this research. This numerical work also corresponds to the experimental work of Ivanov, et al.[17, 20]

4.2 Grid Convergence

A grid convergence study was performed to show that the grids used in this research have a high enough resolution to accurately capture the fluid interactions. The 26° Mach reflection solution was used to compare the coarse, fine, and ultra-fine grids shown in Fig. 3.2. Figure 4.3 shows the coarse mesh converged MR on bottom and the fine mesh converged MR on top. The increased cell density resolves a normal shock on the fine mesh that is 40.3% more compact than its coarse mesh counterpart. As illustrated in the enlarged view, the normal shocks fall within one coarse cell or
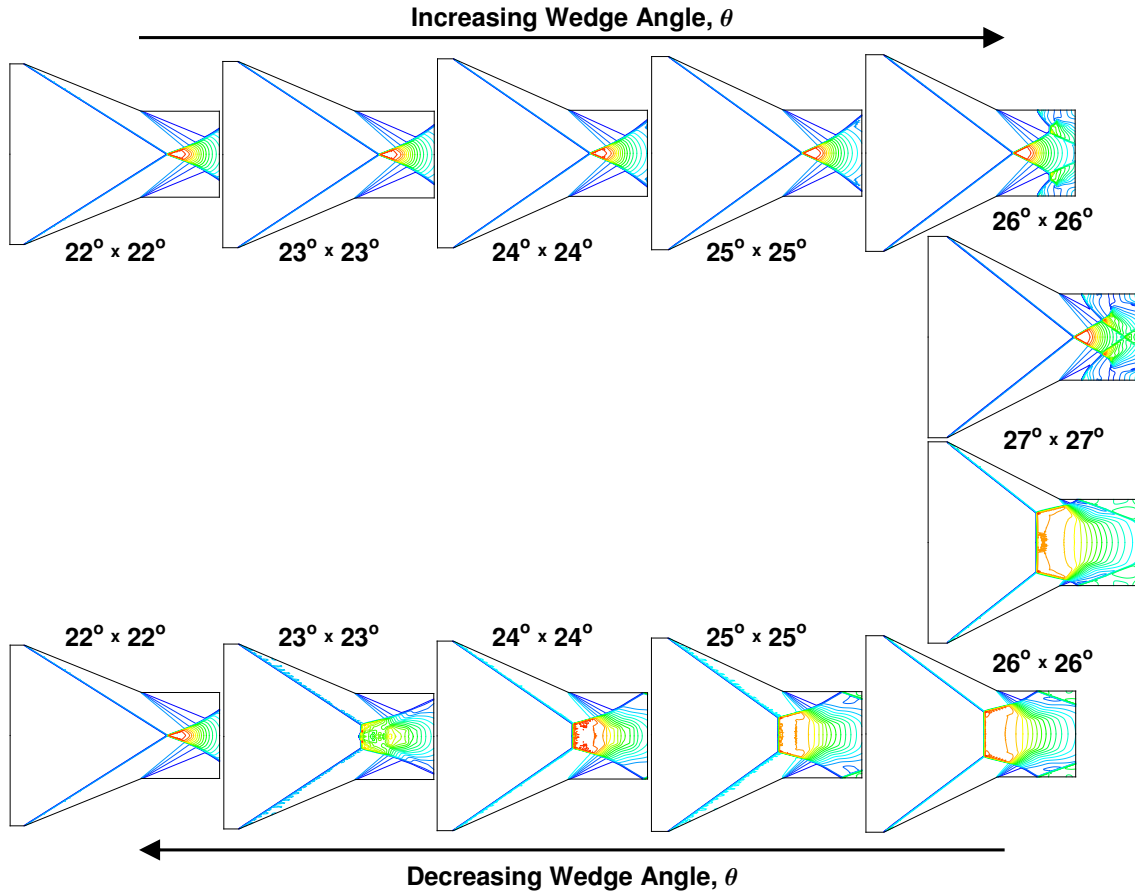
Figure 4.2   Two-dimensional dual-solution domain, $g/w = 0.34$, $M_\infty = 4.96$

two fine cells of each other. The center of the coarse normal shock is 1.72 coarse cells away from the corresponding location on the fine normal shock. This distance is a 2.44% movement. The Mach stem height increases by 2.54% from the coarse to the fine solution. The high correlation between these solutions validates the use of the coarse mesh for preliminary work and trend determination.

The slight difference between the coarse and fine mesh fluid interaction resolution is enough to change the flow behind a regular reflection. Figure 4.4 shows the converged RR for both grids. On bottom, the coarse mesh resolves the primary and secondary oblique shocks, the expansion fan, the shock-expansion fan interactions, and the oblique shock reflections continuing downstream in the inlet, as expected. However, on top the solution resolved on the fine mesh includes an unexpected fea-
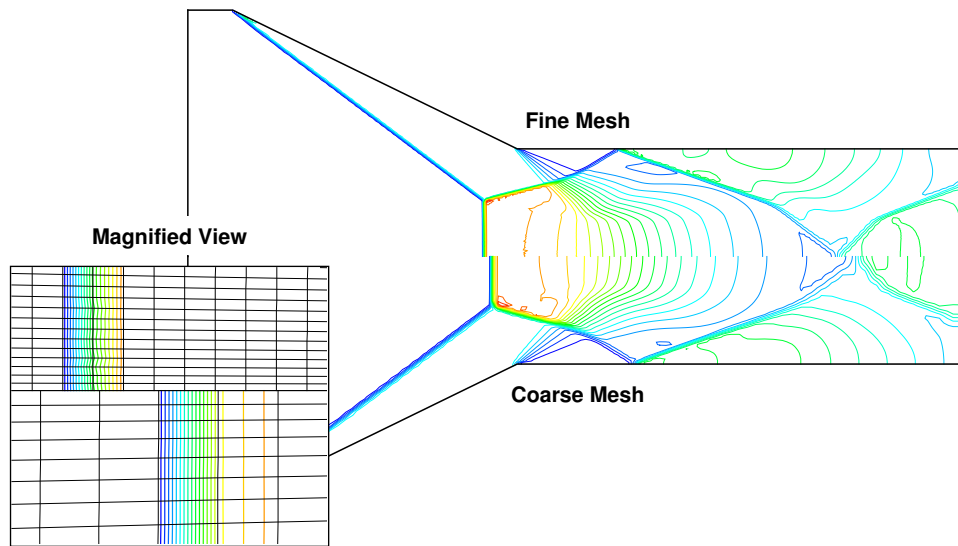
Figure 4.3   MR Pressure contours for coarse, 107×50 on bottom, and fine, 213×99 on top, grids, $26^o \times 26^o$

ture. Instead of traversing the expansion fan and reflecting off the wall, the reflected oblique shock forms a small Mach reflection near the wall.

Figure 4.5 shows u-velocity contours for this 26° RR. The u-velocity remains positive everywhere on the coarse mesh, but a separation region behind the secondary MR is present in the flowfield on the fine mesh. The enlarged view in Fig. 4.5 shows this separation region. This flow phenomena is due to the induced curvature of the reflected shock caused by the shock-expansion fan interaction. The velocity near the wall is accurately resolved by the fine mesh due to the greater cell density in the region near the wall. As the solution converges, the angle of the flow is turned perpendicular to the wall. The wall slip BC sets the velocity tangent to the wall. In this case, as the flow is turned perpendicular, the velocity on the wall decreases. When the velocity becomes subsonic, a shock develops. Once the shock is formed, a larger region of flow is reduced to subsonic velocities. In order to support this increase in subsonic flow, the shock moves forward causing a separation to occur. The pressure change across the oblique shocks grows too large, and a Mach reflection develops. This phenomena does not develop on the coarse mesh due to the lower resolution.
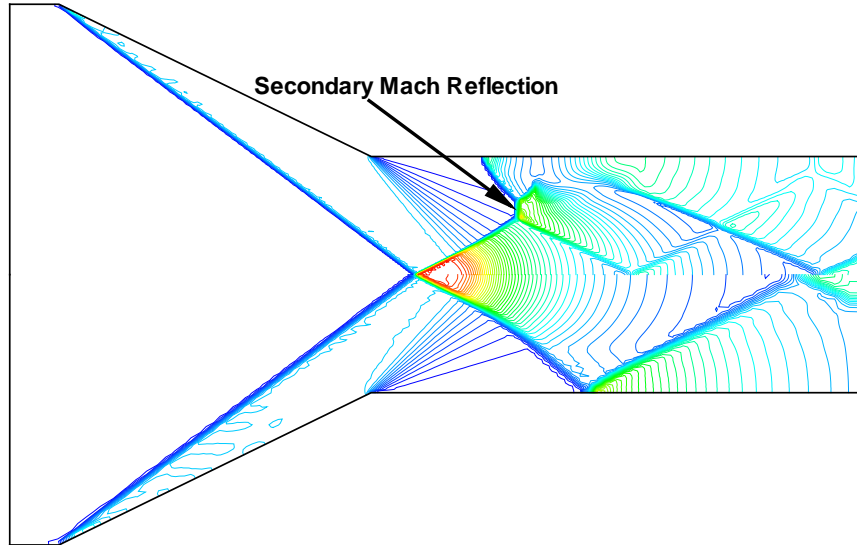
Figure 4.4   RR pressure contours for coarse and fine grids on bottom and top, respectively, $26^o \times 26^o$

In addition, this secondary Mach reflection only appears in regular reflections where $\theta \geq 26^o$.

Figure 4.6 shows the fine mesh converged MR on bottom and the ultra-fine mesh converged MR on top. The ultra-fine normal shock is 51.2% more compact than the normal shock resolved on the fine mesh. The center of the fine normal shock is 1.2 fine cells away from the center of the ultra-fine normal shock, corresponding to a movement of 1.07%. The enlarged view depicts normal shocks that virtually overlap. Figure 4.6 shows good agreement between the fine and ultra-fine mesh solutions with the Mach stem height increasing by 0.87% from the fine to ultra-fine solution. Since the ultra-fine mesh required approximately five times longer to converge than the fine mesh, the fine mesh was chosen as the primary mesh for this numerical study. A
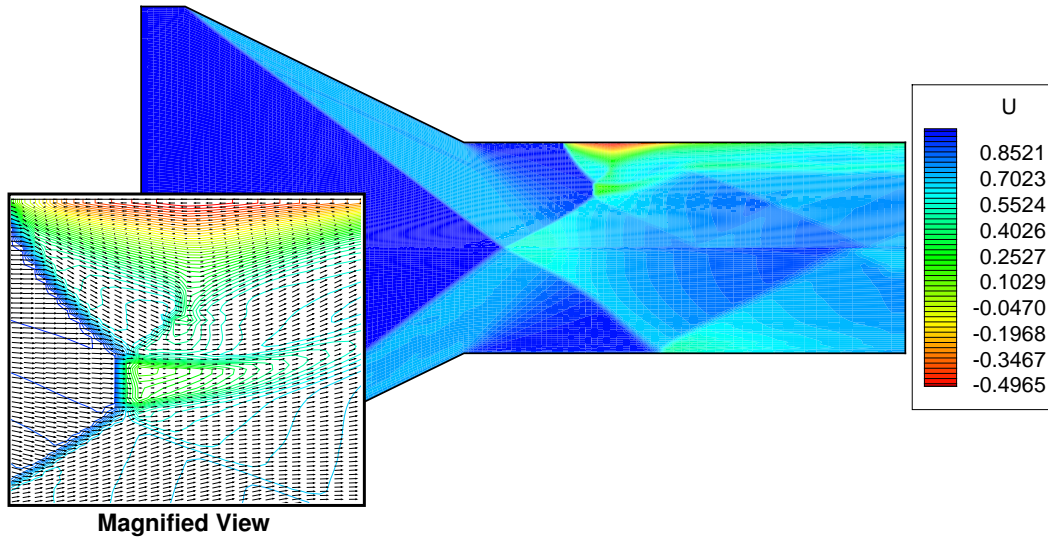
Magnified View

Figure 4.5   RR u-velocity contours for coarse and fine grids, on bottom and top, respectively, $26^o \times 26^o$ (Fine-Magnified)

fine mesh was used for all solutions presented through the rest of this section unless otherwise noted.

4.3   Decelerating Lorentz Force

In order to determine the regular reflection flowfield's sensitivity to transition to Mach reflection, the 25° RR flowfield shown in Fig. 1.5 was subjected to a decelerating Lorentz force as defined in Fig. 3.5. The MGD force was specified by the conductivity pattern of case 2.1.1(Fig. 3.8), a small bread loaf pattern focused over the 26° MR. To accomplish this deceleration, the magnetic field was applied in the $+y$ direction and the interaction parameter was set to 1.0. Figure 4.7 shows the solutions as the decelerating force was applied for a non-dimensional time, τ, of 0.02, 0.05, 0.1, 0.2, and 0.3 which correspond to 2.36×10^{-5} s, 5.9×10^{-5} s, 1.18×10^{-4} s, 2.36×10^{-4} s, and 3.54×10^{-4} s, respectively. The time step, Δt, was 1.18×10^{-6} s, $\Delta \tau = 0.001$. Each inlet represents a snapshot of the flowfield at the specified τ with the force applied. In Fig. 4.7, the bottom half of each inlet is the 25° RR and the top half shows the effect of the force on the RR. Force applications less than $\tau = 0.02$ have no visible

4-6
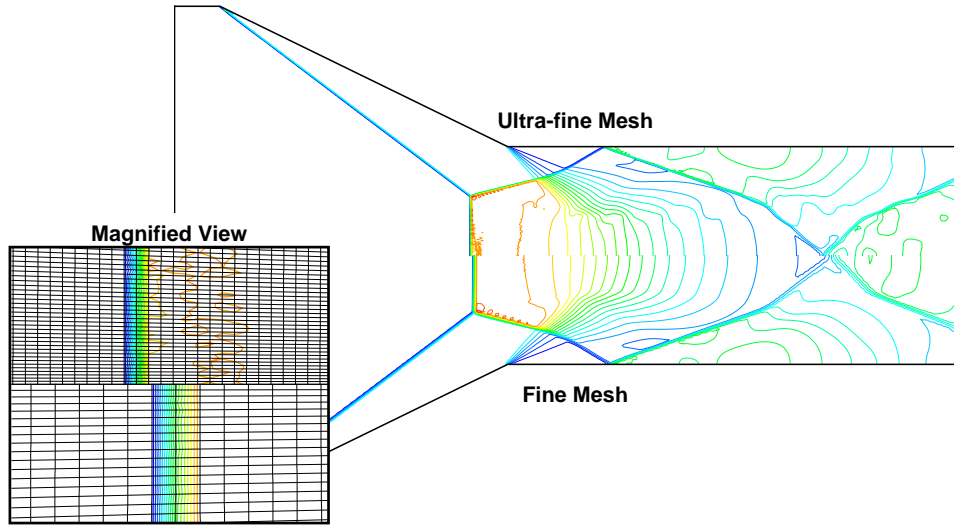
Figure 4.6   MR Pressure contours for fine, 213×99 on top, and ultra-fine, 425×197 on bottom, grids, $26^o \times 26^o$

effect on the the initial and reflected oblique shocks. A decelerating Lorentz force applied for $\tau = 0.05$ moves the reflection point of oblique shocks upstream, beginning the transition to a normal shock in the middle of the inlet. This movement is due to the decrease in the local Mach number to 3.12. The lower local Mach number increases the oblique shock angle β. As the time of force application increases, the pressure contours move upstream and form a normal shock. The pressure contours of the $\tau = 0.3$ solution are aligning at the location of the 25° MR as shown in Fig. 1.6. This decelerating Lorentz force destabilizes the regular reflection enough in $2.36 \times 10^-5\ s$ to transition the desirable RR shock system to the inefficient Mach reflection.

Figure 4.8 compares two solutions with the decelerating Lorentz force applied for $\tau = 0.02$. The top solution is 200 iterations of the decelerating force with a $\Delta\tau = 0.0001$ and the bottom solution is the same force after 20 iterations of $\Delta\tau = 0.001$. The excellent agreement between the two solutions shows that this MGD application is independent of time step.

Figure 4.7   Comparison of the RR movement due to a decelerating Lorentz force
             with increasing τ (RR-bottom, MGD-top)

When the results of the decelerating force were subjected to closer examination, the sensitivity of the regular reflection to transition was easily observed. The pressure contours of the RR have moved upstream when $\tau \geq 0.05$. This movement of the shock system signifies the beginning of the transition to a MR as shown in Fig. 4.7. Decelerating Lorentz force applications less than 2.36×10^{-5} s did not destabilize the RR, and the regular reflection shock configuration remained even after the force was removed. For force applications of $\tau \geq 0.02$, but less than or equal to 0.7, the shock system transitions to Mach reflection when the force is removed. These MRs formed by the decelerating Lorentz force compare favorably with the 25° MR. Figure 4.9

τ = 0.02 by Δτ = 0.0001

Magnified View

τ = 0.02 by Δτ = 0.001
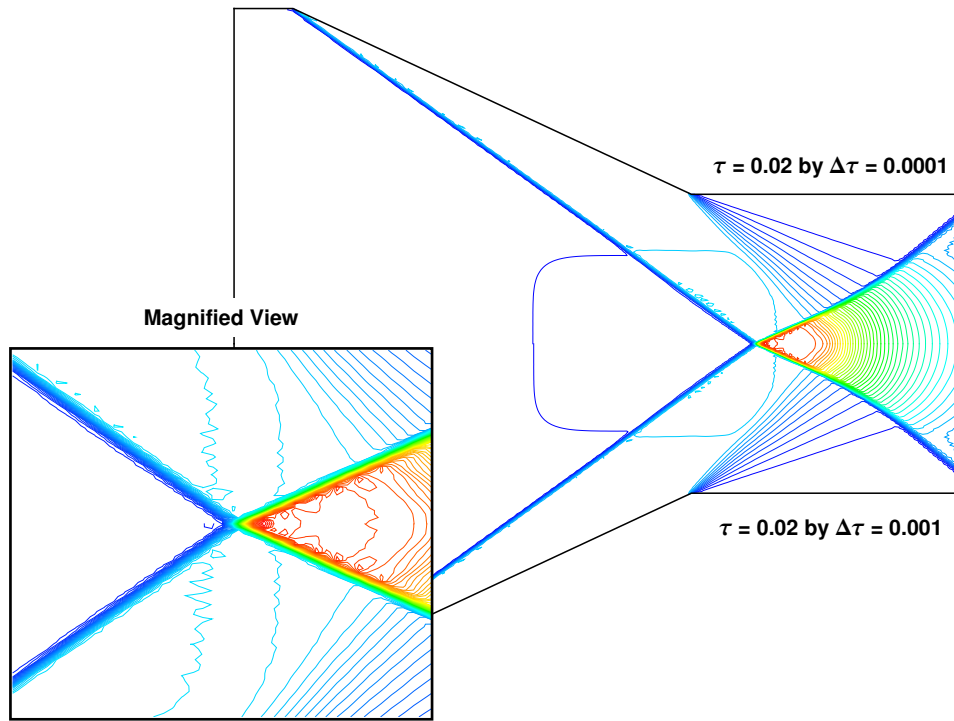
Figure 4.8   Decelerating Lorentz force Time Step comparison pressure contours, $25^o \times 25^o$

shows the 25° converged MR on bottom and the MR formed by a decelerating Lorentz force applied for $\tau = 0.1$ on top. The regular reflection is extremely sensitive to the disturbance created by this decelerating Lorentz force. The inlet sustains higher total pressure losses and a lower compression ratio due to this RR transition to MR, and a higher probability of inlet unstart.

The inlet unstarts when the decelerating Lorentz force is applied to the regular reflection for longer than 8.267×10^{-4} s, $\tau = 0.7$. The rate of this inlet unstart is dependent upon how long the force is applied. Figure 4.10 demonstrates the effects of the decelerating force when the application period was increased beyond those shown in Fig. 4.8. The 25° MR is shown on the bottom of each inlet and the decelerating Lorentz force solution for each τ is shown on top. When the force is applied for $\tau > 0.3$, the shock structure is moved upstream beyond the 25° MR. A decelerating Lorentz force applied longer than 8.267×10^{-4} s created a normal
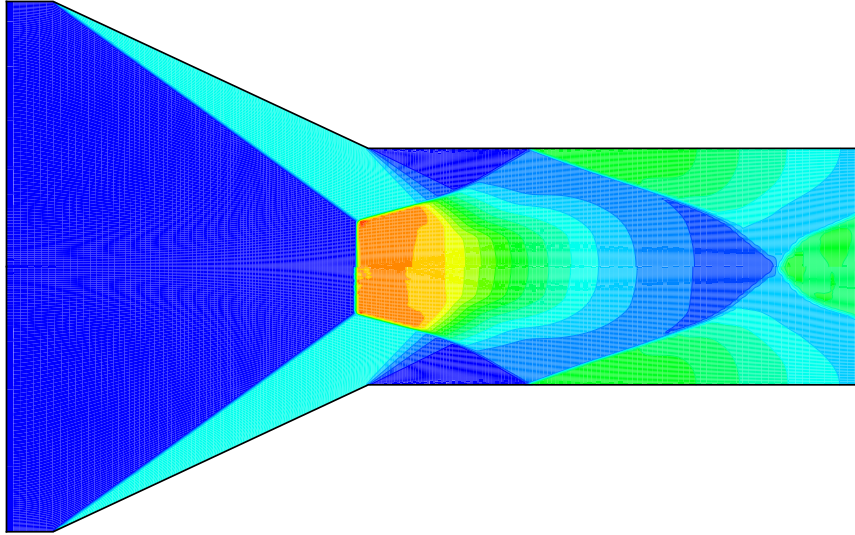
Figure 4.9   MR formed by a decelerating Lorentz Force (25° MR-bottom, MGD MR-top)

shock that propagates to the entrance of the inlet. This shock system was expelled even if the force was removed. The inlet unstart dramatically reduces the thrust of the SCRAMjet and increases the drag. Figure 4.11 illustrates inlet unstart due to a decelerating Lorentz force. The force was applied for $\tau = 1.5$, 1.771×10^{-3} s, and then removed. The inlet unstarts as the flowfield converges.

The regular reflection is extremely sensitive to any upstream disturbance, transitioning to a Mach reflection almost immediately. Transient application of the decelerating Lorentz force for microseconds transitioned the RR to the inefficient MR shock configuration. The higher total pressure losses and reduced compression ratio of this MR configuration will reduce the thrust of a SCRAMjet. Applications of this force for milliseconds resulted in inlet unstart.
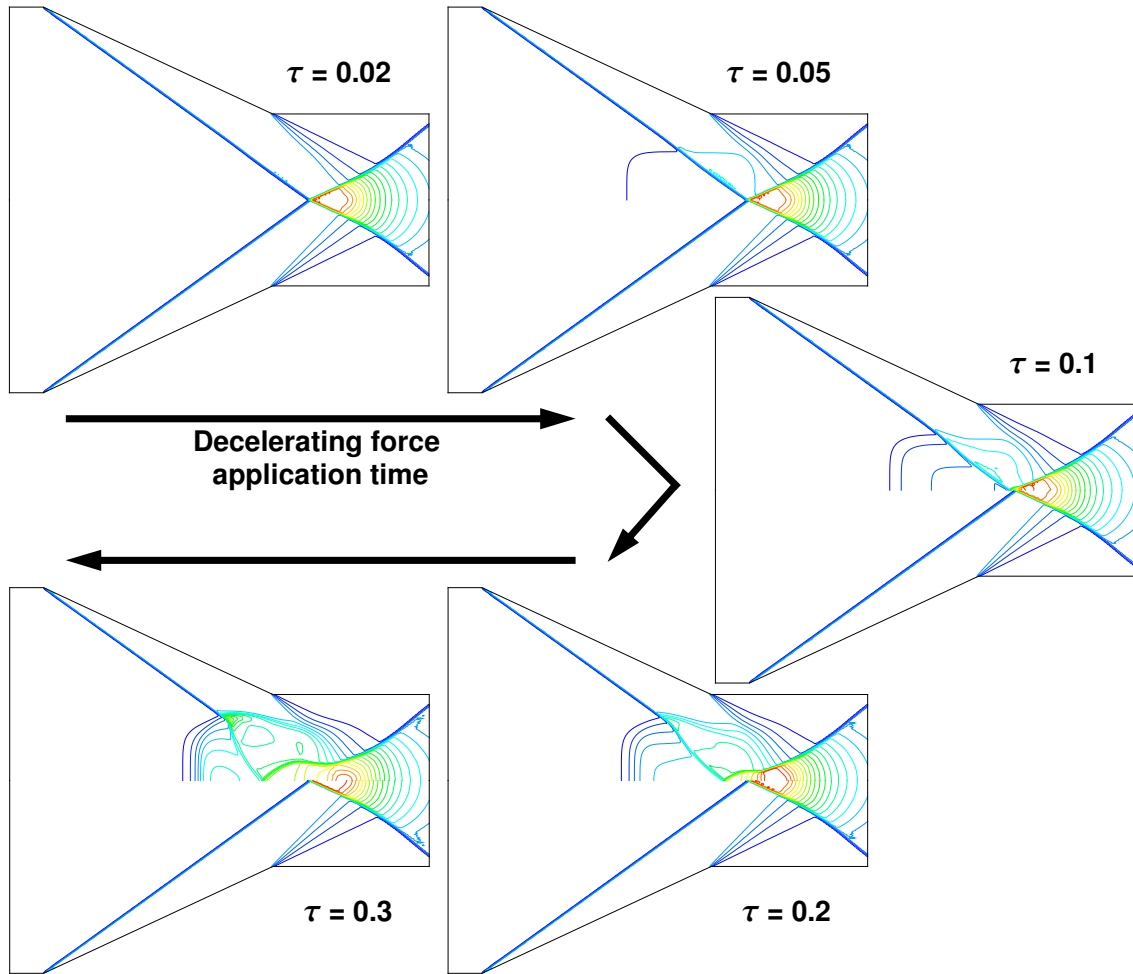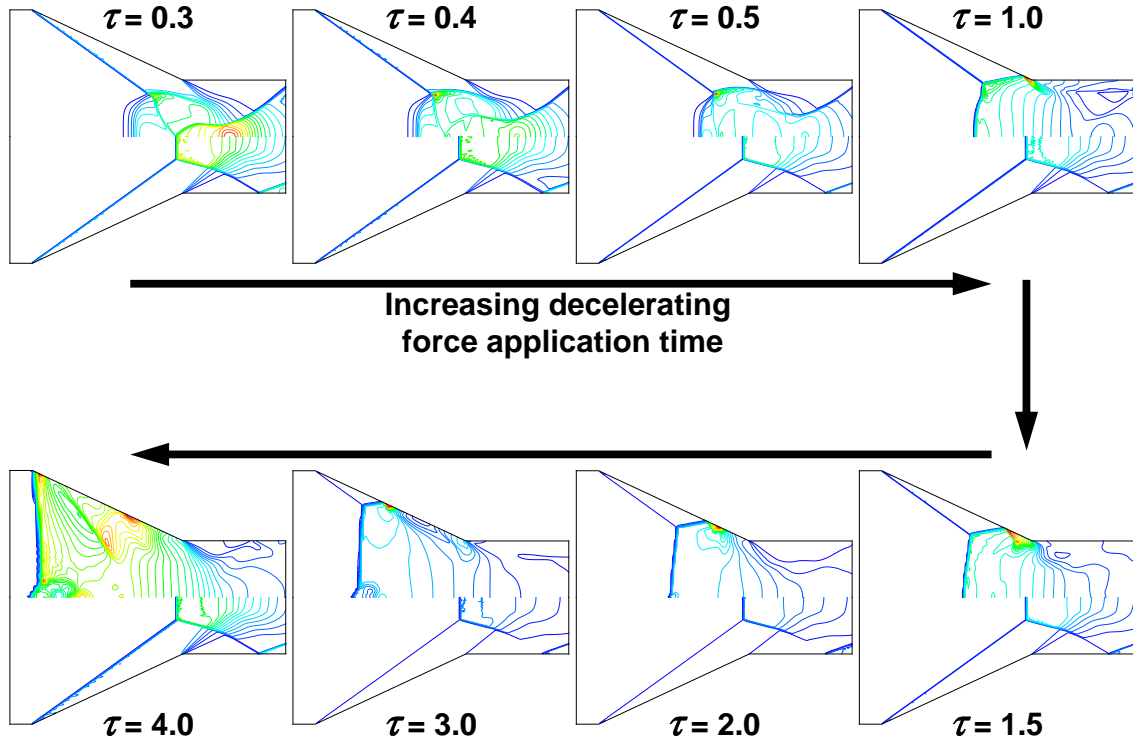
Figure 4.10   Comparison of the RR movement due to a decelerating Lorentz force
with increasing τ (25° MR-bottom, MGD-top)

4.4   Accelerating Lorentz Force

This numerical study investigates the use of the interaction between electro-
magnetic fields and a conductive flowfield to reduce the inefficiencies in a SCRAMjet
inlet created by the transition of a regular reflection to a Mach reflection. The 26°
MR was subjected to an accelerating Lorentz force with the goal of reducing these
inefficiencies and possibly transitioning the MR to a RR. The accelerating Lorentz
force was created by applying a magnetic field in the $-y$ direction and an electric
field in the $+z$ direction as shown in Fig. 3.6. This MGD force was applied in the
region specified by the conductivity (Eqn. 3.25). The region of conductivity was
varied through all of the cases presented in Table 3.1 and shown in Figures 3.8, 3.9,
and 3.10. These cases were numerically implemented on the coarse mesh to decrease
the computational time required in determining the optimum conductivity case.

4-11
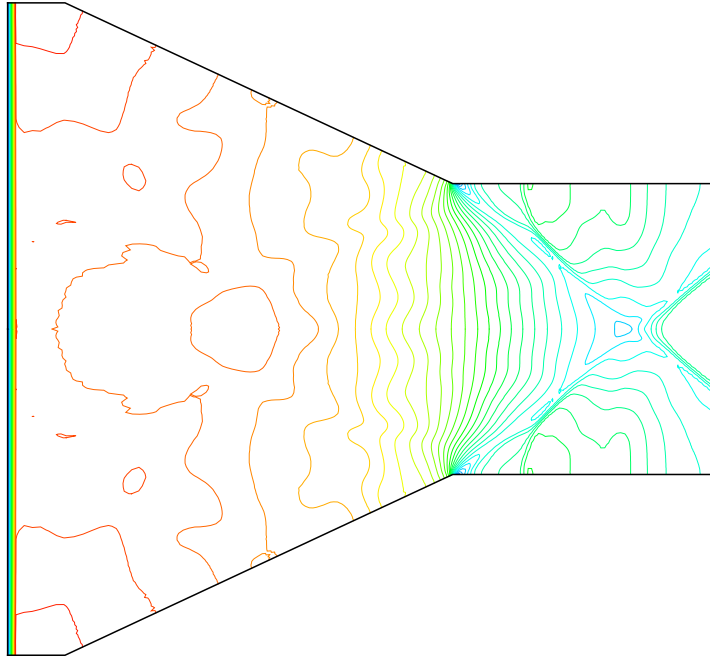
Figure 4.11   Inlet unstart due to a decelerating Lorentz Force

The area where the accelerating Lorentz force acts is determined entirely by the conductivity pattern. A pattern completely in front of the Mach reflection only accelerates the fluid before it passes through the normal shock. The patterns entirely behind the Mach reflection accelerate the fluid downstream of the normal shock, and the fluid upstream of the shock system is not influenced by this acceleration. In both cases, one would expect the limited application of the accelerating force to have very little effect on the shock system. Centering the accelerating Lorentz force over the MR accelerates the fluid upstream and downstream of the normal shock. The MR location should push the MR downstream further and reduce the Mach stem more than either of the other two application locations. Applying the force over greater areas of the flowfield in both length and width increases the energy addition to the flow. This greater energy addition should result in greater acceleration and greater MR movement. The optimum conductivity pattern should have the greatest

4-12

downstream movement of the normal shock without inducing flowfield distortion, such as the secondary MRs.

The optimum σ pattern was implemented and the interaction parameter was varied from 1.0 to 10.0 to determine its effect on the MR flowfield. The increases in $\mathcal{Q}$ represent increases in the applied magnetic field. The source term on the continuity of momentum equation is $\mathcal{Q}(\vec{j} \times \vec{B})$ and the magnitude of the applied magnetic flux is defined:

$$B_0 = \sqrt{\frac{\mathcal{Q}\rho_0 V_0}{\sigma_0 L_0}} \tag{4.1}$$

The current, $\vec{j}$, increases linearly with the magnetic flux. The combination of these effects specifies that the magnitude of the Lorentz force goes with $\mathcal{Q}^2$. Increases in the interaction parameter should result in a more effective force, magnifying the changes created in the flowfield.

The load factor was varied independent of the interaction parameter to determine its effect on the MR. $\mathcal{K}$ was increased from the nominal values of 1.2, to 1.8 and then to 2.4, increases of 50% and 100%, respectively. The increases in $\mathcal{K}$ represent increases in the applied electric field. The force should increase linearly with the load factor because the current increases linearly with the electric field. This increase is rapidly offset by the square relationship between the heating and $\mathcal{K}$. The increases in the load factor should actually be detrimental to the flowfield. The greater Lorentz force will not be able to offset the greater heating and the MR will move upstream, or the inlet could possibly unstart.

The mass-averaged static pressure increases by a factor of 22.18 through the shock structure of a 26° regular reflection at $M_\infty = 4.96$. The Mach reflection for identical conditions only compresses the flow by a factor of 19.68, 11% less than the RR compression ratio. The mass-averaged total pressure ratios across 26° RR and MRs are 0.283 and 0.249, respectively. The transition from RR to MR also moves

the shock system upstream 23% to a less stable location in front of the throat. Use of an accelerating Lorentz force to trigger the transition to a RR is desirable because of this 12% loss in total pressure recovery and 11% reduction in compression. This force would reduce the total pressure losses associated with the normal shock of a MR and provide better flow compression with the transitioned RR. Additionally, this force has the capability to prevent potential engine inlet unstart due to the instability of the MR.

4.4.1   Specification of Conductivity.   The coarse mesh is used to demonstrate the overall effects of the ten conductivity patterns used in this research(Table 3.1). While the results are less accurate than those on the fine mesh, the general trends are duplicated. Fewer nodes decrease the computational time required for convergence. For this numerical study, the conductivity pattern that provides the largest reduction in the Mach reflection without overly distorting the flowfield is the most desirable pattern. The feasibility of creating this field is not examined.

Figure 4.12 illustrates the effect that changing the conductivity specification has on the flowfield. The 26° MR is shown on the bottom of each inlet and the flowfield with the $\mathcal{Q} = 3.0$ accelerating force is presented on top. The focused conductivity, case 2.1.1, has a very large effect on the MR pushing the normal shock downstream to a position that is 34.57% of the difference between the 26° Mach and regular reflection locations. The Mach stem height is reduced also. Application of this conductivity pattern also destroys the reflection pattern further downstream developing a new Mach reflection near the wall. These flowfield effects are the result of the flow directly in the center of the inlet accelerating with little or no change in the flow outside the σ concentration, creating effects much like a jet.

In case 2.2.1 the conductivity is focused directly over the MR and is gradually reduced near the walls. Figure 4.12 illustrates that this σ pattern results in a MR moved further downstream than the case 2.1.1, reducing the distance between the

Case 2.1.1

Case 2.2.1

Case 2.2.2

Case 2.3.1
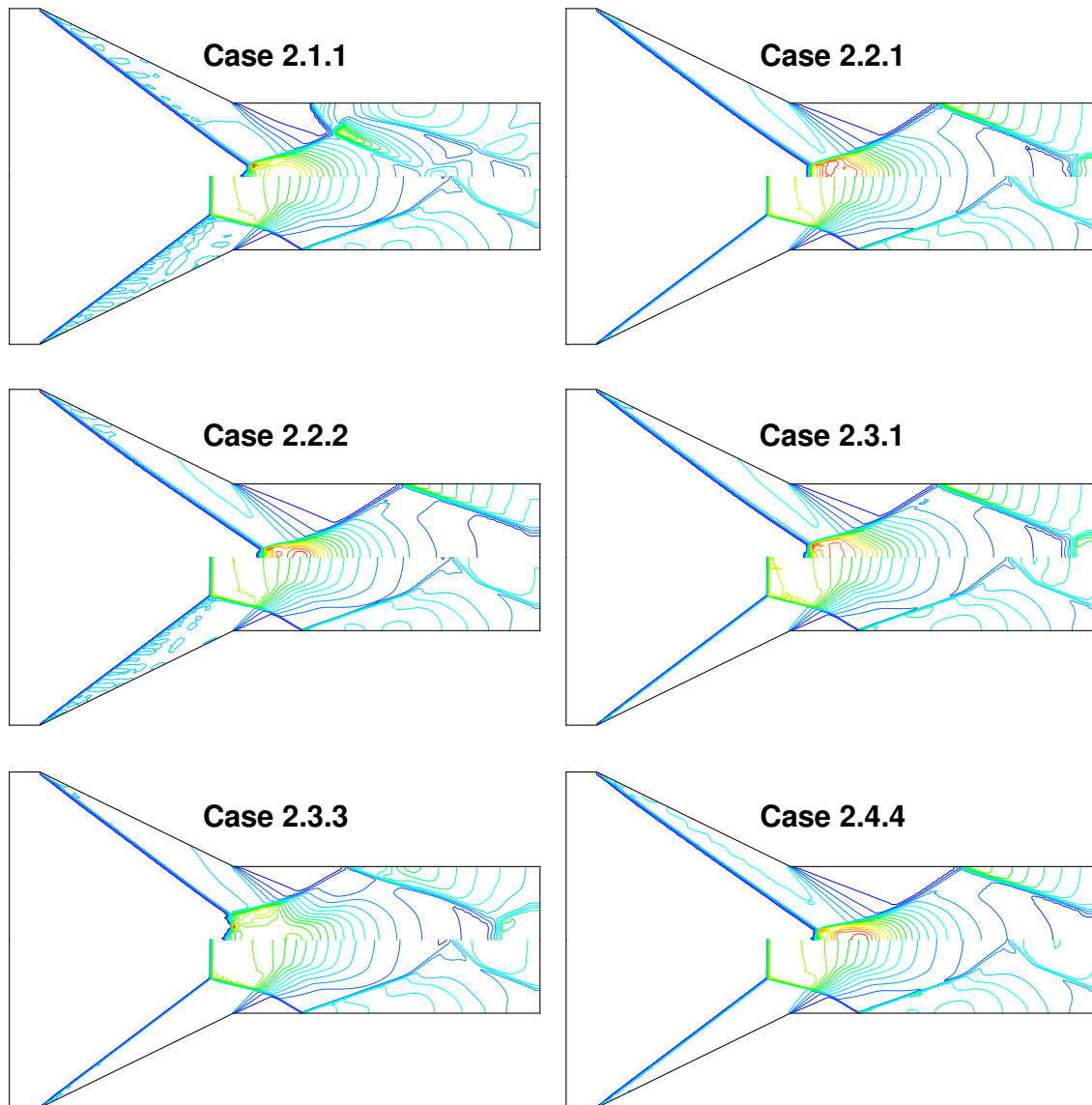
Case 2.3.3

Case 2.4.4

Figure 4.12   Contours of pressure with $\mathcal{Q} = 3.0$, conductivity centered at the 26° MR, Cases 2.1.1, 2.2.1 , 2.2.2, 2.3.1, 2.3.3, 2.4.4, Coarse Mesh (MGD-top, MR-bottom)

MR and RR by 84%. The greater movement is accomplished without the flowfield degeneration of case 2.1.1. The flowfield when σ spans the entire width of the inlet, 2.3.1, is very similar to 2.2.1. The normal shock is moved almost as far downstream to a location that is 16.87% of the original. The reduced length specification in case 2.3.3 greatly decreases the impact of the accelerating force, only moving the normal shock downstream 30%. These cases with greater width specification do not create the jet effect of case 2.1.1 because the flow all the way across the inlet is accelerated. The reduced length of the 2.3.3 pattern accelerates the flow for a shorter period and correspondingly has less effect.

Cases 2.2.2 and 2.4.4, the gradient full and constant σ specifications respectively, have the greatest impact on the Mach reflection as shown in Fig. 4.12. The MR is moved to a location 0.83% downstream of the 26° RR, a 100.83% movement for case 2.2.2. In this case the conductivity is a constant 1.0 for most of the flowfield and gradually tapers down at the entrance and exit of the inlet. A constant $\sigma = 1.0$ throughout the flowfield, case 2.4.4, moves the MR downstream to a location 95.8% of it original location. The accelerating force in both cases induces none of the added flowfield distortion present in the center focused pattern, case 2.1.1. The flowfield in both cases is uniformly accelerated in width and length, accelerating the flowfield more than the other cases.

The effects of the accelerating Lorentz force are very similar for σ cases 2.2.2 and 2.4.4. Figure 4.13 shows the gradient full pattern on bottom and the constant σ on top. The gradient full conductivity pattern moves the normal shock further downstream than the constant σ. This movement corresponds to a smaller Mach stem. While case 2.2.2 and 2.4.4 are similar, Fig. 4.14 illustrates that the gradient specification is the more optimum of the two. Case 2.2.2 is on the bottom of the inlet and case 2.4.4 is on top. The constant σ pattern has a greater maximum temperature, and greater temperature rise overall, than the gradient full pattern. The gradient pattern adds less energy to the flowfield. As soon as the flow enters

the inlet, the constant σ pattern adds the maximum energy to the flow. This high input shows up in the temperature rise.
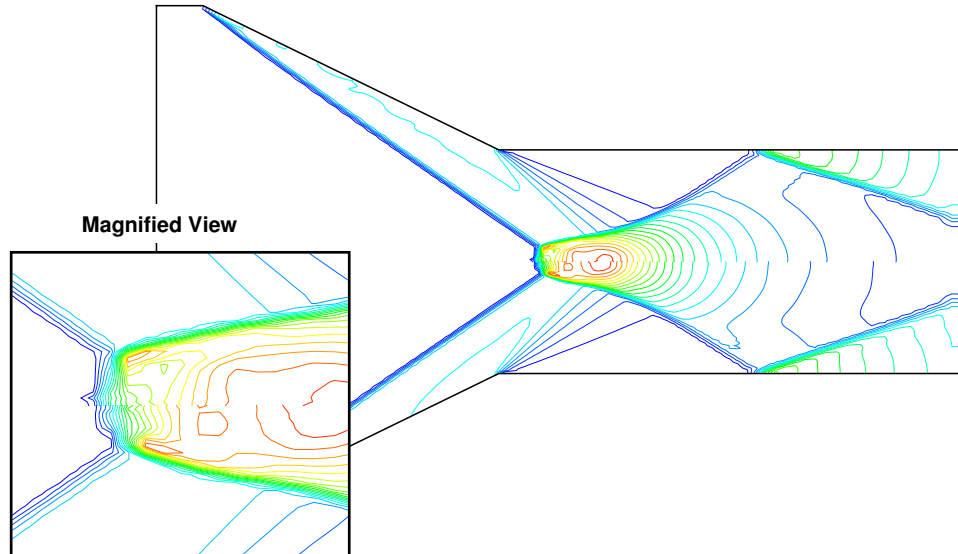
Figure 4.13   Contours of pressure with $\mathcal{Q} = 3.0$, Case 2.2.2 on bottom and case 2.4.4 on top on the coarse Mesh

Figure 4.15 shows the effects of the accelerating force when the force is applied in front of the MR. Cases 1.1.1 and 1.2.1 are shown at the top of the inlets and the 26° MR is on the bottom. Both conductivity patterns effect the flowfield, but the effects of the accelerating Lorentz force are less than the MR centered patterns when the force is applied in front of the Mach reflection. Case 1.1.1 moves the normal shock downstream 22.45% and case 1.2.1 moves the normal shock to a location that is 19.93% less than the original value. The Mach stem height is reduce accordingly for both cases. The focused pattern, case 1.1.1, distorts the flowfield slightly more, as expected, due to the center focus of the accelerating force like case 2.1.1.

Figure 4.16 shows the effects of the accelerating force when it is applied behind the MR. The accelerating MGD force is depicted at the top of the inlets and the 26° MR is on the bottom. The rear location has very little effect on the shock system for either pattern, moving the MR back 12.34% in both cases. These minimal changes are due to application of the accelerating force behind the normal shock in both
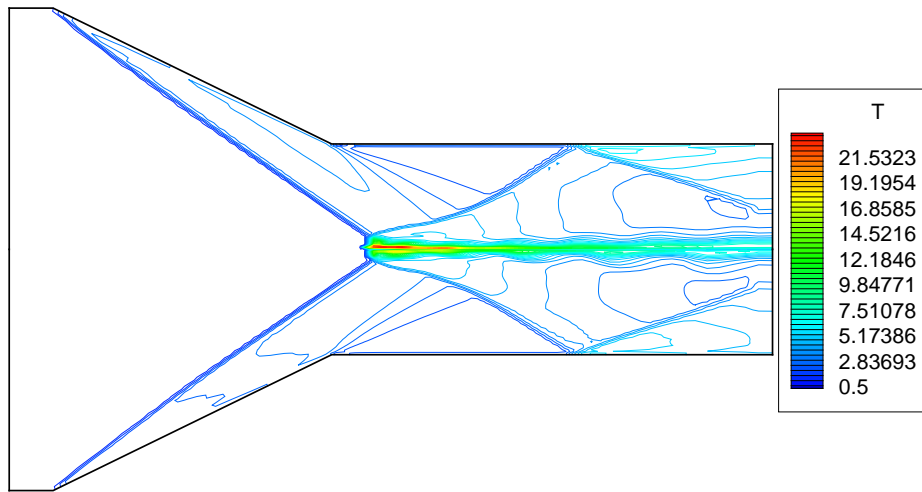
Figure 4.14   Contours of temperature with $\mathcal{Q} = 3.0$, Case 2.2.2 on bottom and case 2.4.4 on top on the coarse Mesh
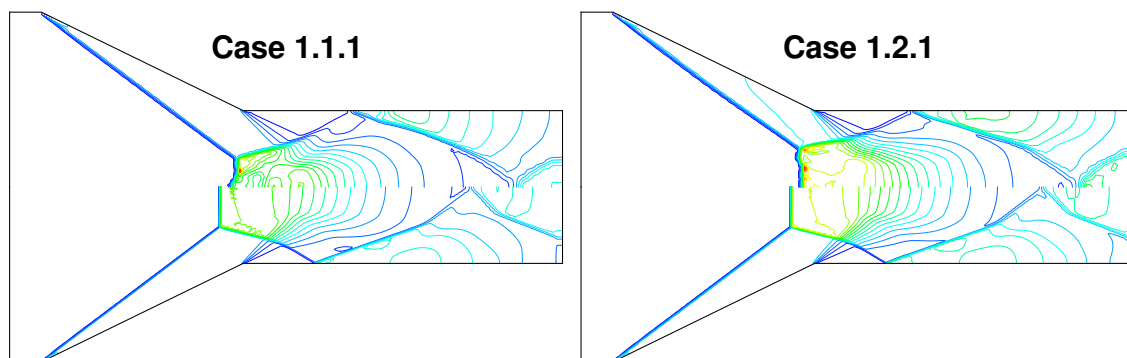

Figure 4.15   Contours of pressure with $\mathcal{Q} = 3.0$, conductivity centered in front of the 26° MR, Cases 1.1.1, 1.2.1, Coarse Mesh (MGD-top, MR-bottom)

conductivity patterns. The supersonic flow upstream of the shock system can not respond to the downstream application.
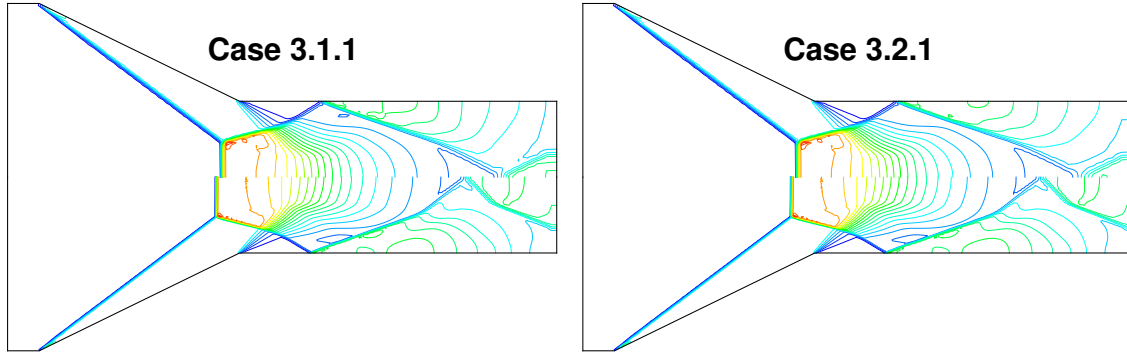

Figure 4.16   Contours of pressure with $\mathcal{Q} = 3.0$, conductivity centered behind the 26° MR, Cases 3.1.1, 3.2.1, Coarse Mesh (MGD-top, MR-bottom)

The effects of the conductivity pattern are independent of the interaction parameter. The gradient full conductivity pattern, case 2.2.2, has a greater effect on the Mach reflection and less flowfield distortion than the focused conductivity, case 2.1.1, regardless of the value of $\mathcal{Q}$. Figure 4.17 compares these two conductivity patterns at interaction parameters of 1.0, 3.0, and 5.0. All inlets have the gradient full pattern on top and the focused pattern on bottom. For the equivalent interaction parameter, the Mach reflection is moved much further downstream by the gradient full pattern. The temperature contours illustrate the severe problems created by the center focused σ pattern. Case 2.1.1 with $\mathcal{Q} = 3.0$ creates non-dimensional temperatures in excess of 1850.0. In order to show any of the temperature contours for case 2.2.2 with $\mathcal{Q} = 3.0$, the temperature contours for the whole $\mathcal{Q} = 3.0$ inlet are logarithmic. With the linear scale used on the other inlets only one contour would appear for case 2.2.2 if 30 temperature contours were used because its maximum non-dimensional temperature is 68.67. The maximum temperature for case 2.1.1 when $\mathcal{Q} = 3.0$ is equivalent to a temperature in excess of 135,000 K, well outside the bounds of the ideal gas law. This temperature is beyond the bounds of the models used in this research, but the general trend is correct and the heating encountered using a focused conductivity is excessive. The largest amount of energy added to the

flow occurs along the centerline. By the end of the region of conductivity, the Δe along the center of the inlet is at the maximum value. The $\mathcal{Q} = 3.0$ focused σ MR is located at this point of maximum Δe. The combination of the increased heating due to the added energy and the temperature rise across the normal shock results in the maximum temperature encountered in this research. Heating excesses such as this are outside the models used in the code employed in this research.
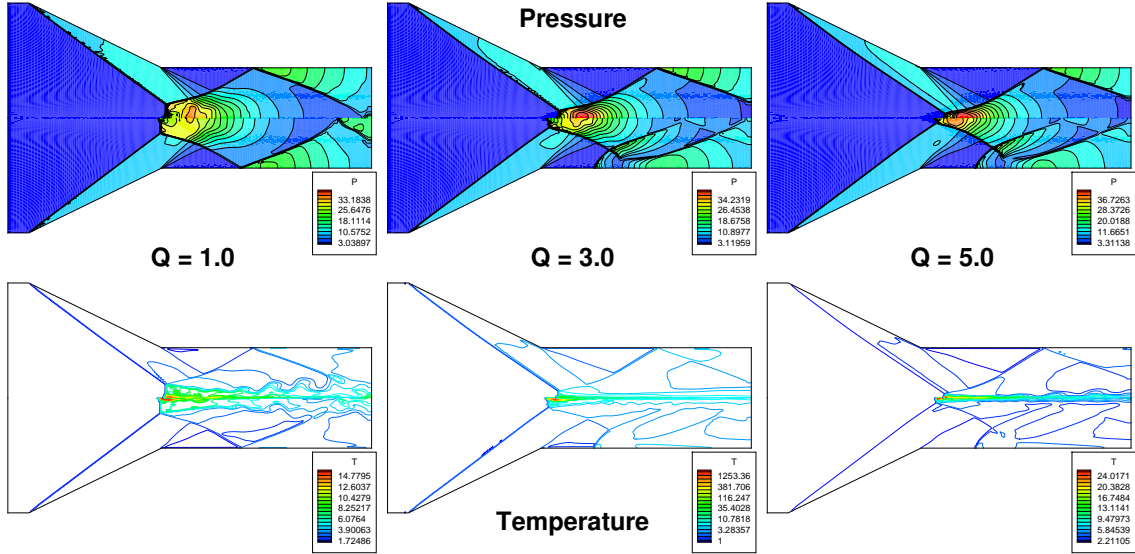
Figure 4.17   Comparison of the MR movement due to an accelerating Lorentz force with increasing interaction parameter values, σ Case 2.1.1 on bottom and case 2.2.2 on top, Fine Mesh

When $\mathcal{Q} = 5.0$, the temperatures for case 2.1.1 are well within the range of the ideal gas law with a maximum value of roughly 2000 K. While these temperatures are outside of the constant γ bounds, the area where the temperature is greater than 800 K is very small, and the presented trends accurate. The MGD code employed for this numerical study is valid for most of the flowfield, but future work might include the capability for a non-constant ratio of specific heats.

The total pressure losses are greater for case 2.1.1 than case 2.2.2 as shown in Fig. 4.18. The gradient full pattern is again presented on the top of the inlet and the focused pattern is on the bottom. The average Mach number is greater when the

gradient full σ pattern is used. The separation region and secondary Mach reflection present in case 2.1.1 are not present in case 2.2.2 on the coarse or fine mesh.
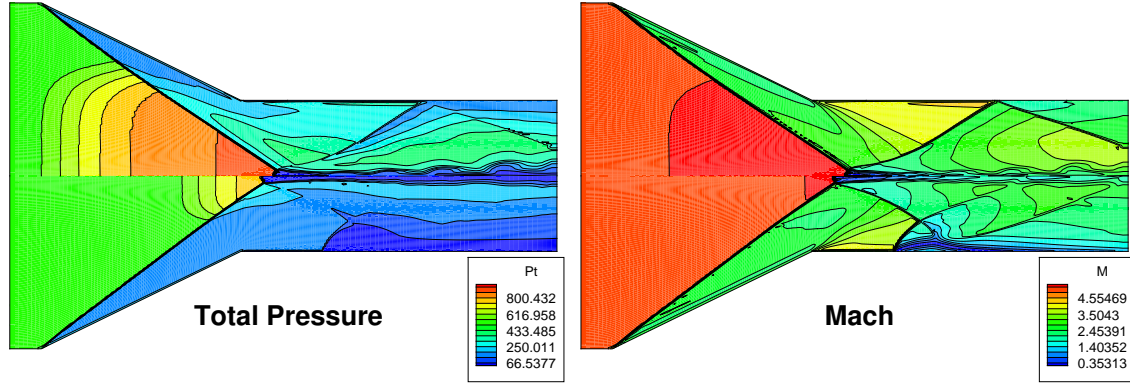
Figure 4.18 $\mathcal{Q} = 5.0$ parallel Lorentz force Mach and total pressure contours, σ Case 2.1.1 on bottom and case 2.2.2 on top, Fine Mesh

The gradient full conductivity pattern is the most effective of the ten conductivity patterns studied in this research and includes the least flowfield degradation. Unless otherwise specified, case 2.2.2 is used for the rest of this section.

4.4.2   Magnetic Field Magnitude.   In order to try to transition the MR to a RR, the converged 26° MR solution was subjected to an accelerating Lorentz force with interaction parameters from 1.0 to 10.0 and the conductivity specified by case 2.2.2. The load factor remained at the nominal value of 1.2 specified by $E_0 = 1.2$. When the accelerating Lorentz force was acting parallel to the flow, the 26° MR moved downstream through the throat to a new location 47.55% of the original MR location when $\mathcal{Q} = 1.0$. Figure 4.19 illustrates the changes in the MR due to the applied force. In this figure, the 26° RR solution is depicted on the bottom of the flowfield, and the MR with application of the accelerating Lorentz force is depicted on top. As the interaction parameter is increased from 1.0 to 10.0, the magnitude of the applied magnetic field is increased, and the MR moves further downstream.

While the Mach reflection is pushed beyond the location of the regular reflection, the MR is not fully transitioned to a RR reflection in Fig. 4.19. The shock
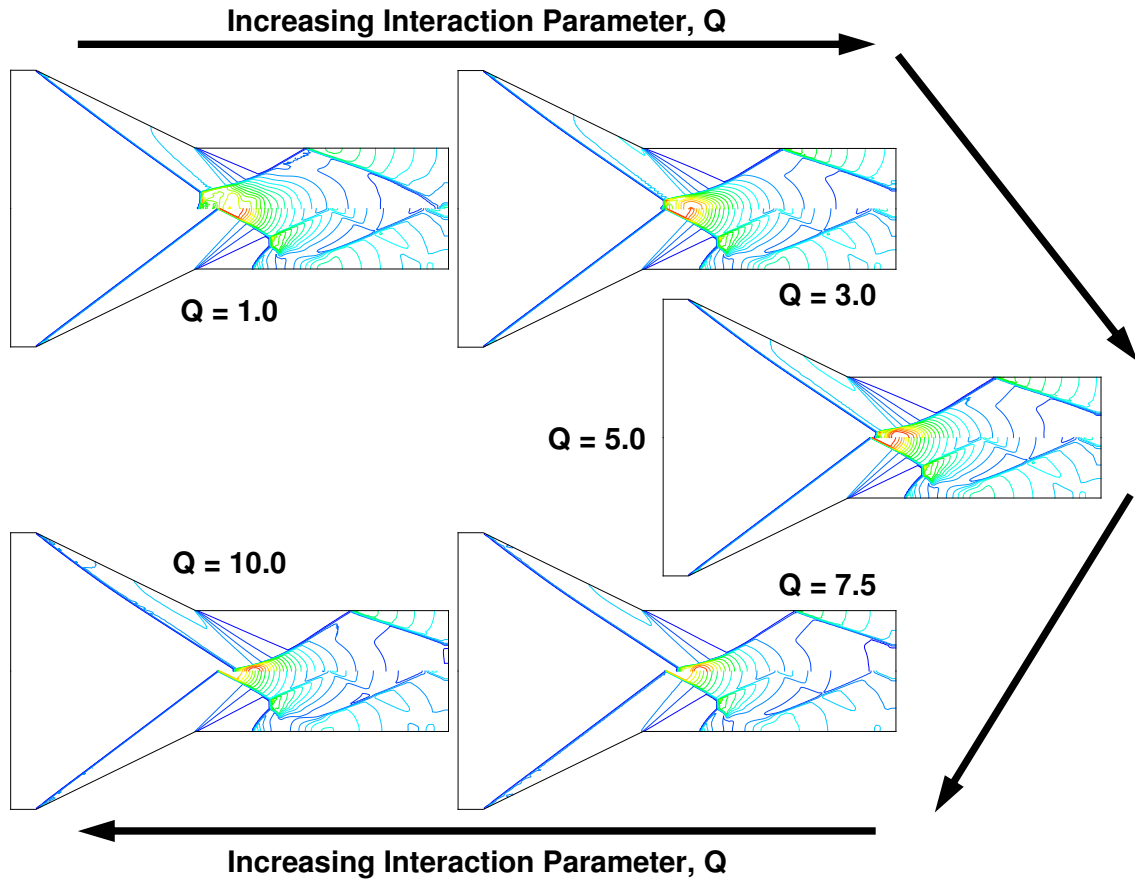
Figure 4.19   Movement of the MR due to a parallel Lorentz force with increasing
             interaction parameter values (MGD-top, RR-bottom)

systems of both the $\mathcal{Q} = 7.5$ and 10.0 solutions are pushed downstream well beyond
the location of the 26° RR to new locations that are 27.74% and 36.97% beyond the
regular reflection, respectively. The locations of the new MRs are a result of the the
increased flowfield Mach numbers. By the time the flow reaches the normal shock in
the $\mathcal{Q} = 10.0$ solution, the local Mach number is 5.44. This increased Mach number
results in a lower oblique shock angle, β. Figure 4.20 depicts the $\mathcal{Q} = 10.0$ MR on
top of the each inlet with the 26° MR and RR on the bottom. The top inlets show
contours of Mach number, the middle, contours of pressure, and the bottom inlets,
contours of total pressure. The oblique shock is bent towards the wall due to the
Lorentz force acceleration. The average Mach number and total pressure at the exit
of the inlet is higher in the MGD inlet than the 26° RR inlet. This is dictated by the

energy interaction and Lorentz force source terms in the MGDE. The accelerating Lorentz force increases the velocity of the flow in the region specified by σ. Total pressure is based on pressure and Mach number, and the Mach number increases as the velocity increases. This inter-relation would allow the total pressure to increase through the inlet, given a high enough $\mathcal{Q}$. The 26° RR solution also experiences greater losses in Mach number and total pressure due to the secondary MR.
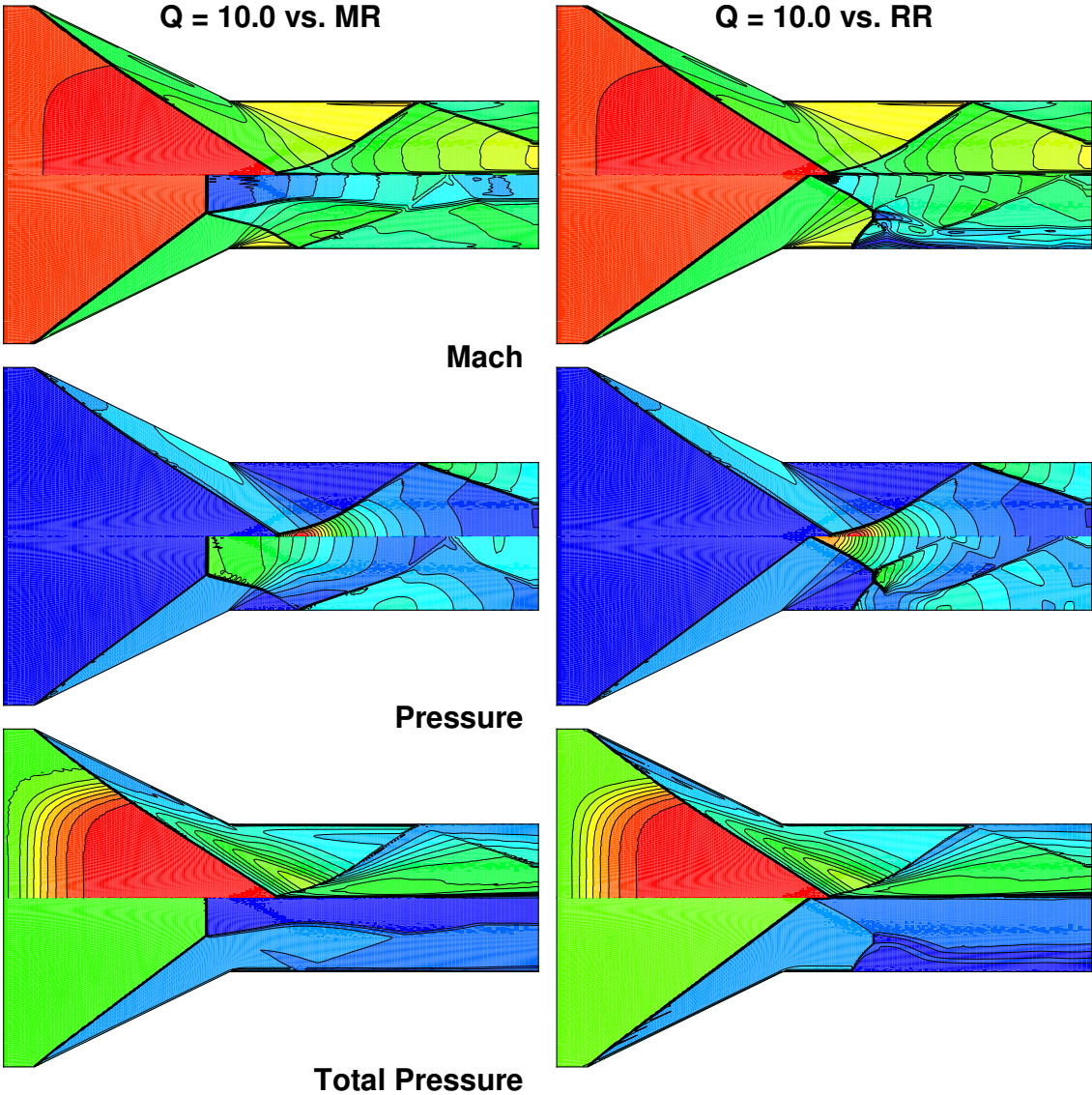

Figure 4.20 $\mathcal{Q} = 10.0$, MR, and RR parallel Lorentz force Mach, pressure, and total pressure contours(MGD-top, MR & RR-bottom)

Figures 4.21 and 4.22 show the regular and Mach reflections respectively, on the bottom of an inlet with the $\mathcal{Q} = 10$ flowfield on top. In the enlarged view, the contours of Mach show that the normal shock is 95% smaller than the 26° MR, but the higher local Mach number induced by the accelerating Lorentz force creates a much stronger normal shock. The flowfield behind the shock structure when $\mathcal{Q} = 10.0$ displays the expected pattern of oblique shock reflections unlike the flowfield behind the 26° RR. The energy added to the flowfield prevents the flow from forming the secondary Mach reflections present in the RR.
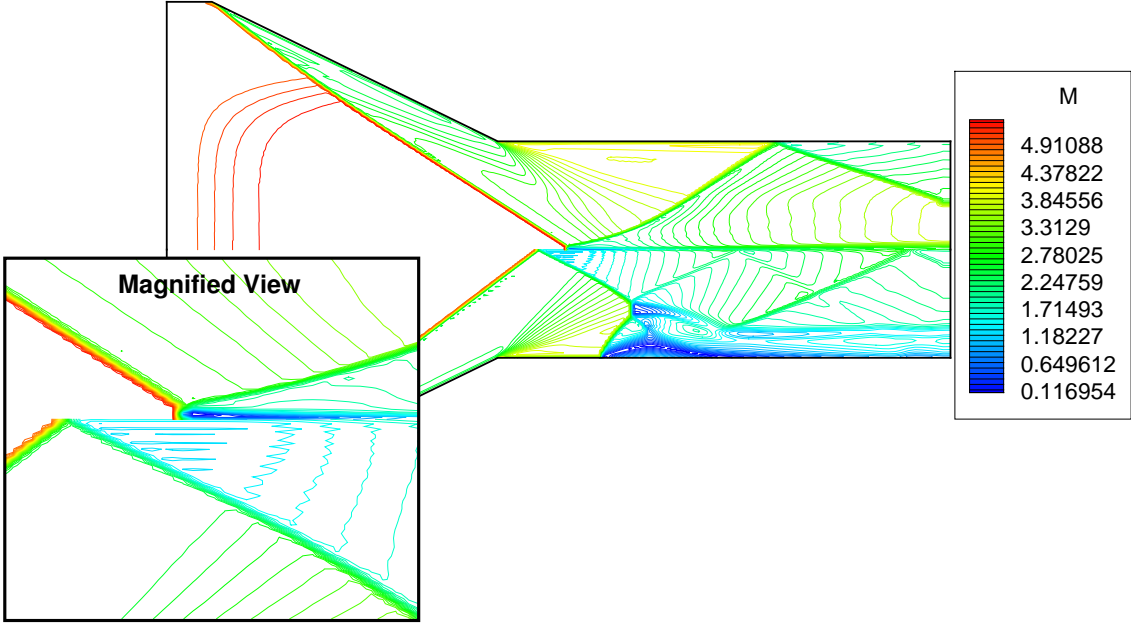
Figure 4.21   Mach contours for $\mathcal{Q} = 10.0$ on top and the 26° RR on bottom

In order to provide a measure of the effectiveness of an accelerating Lorentz force, mass-averaging was used. The location where the data sampling takes place can greatly effect the results of the mass-averaging. The changing location of the shock system makes the sampling difficult in this research. The 26° MR and RR are chosen as the baseline parameters and each solution is sampled behind the throat, at a location 0.12 behind the normal shock or reflection.

Figure 4.22   Mach contours for $\mathcal{Q} = 10.0$ on top and the 26° MR on bottom
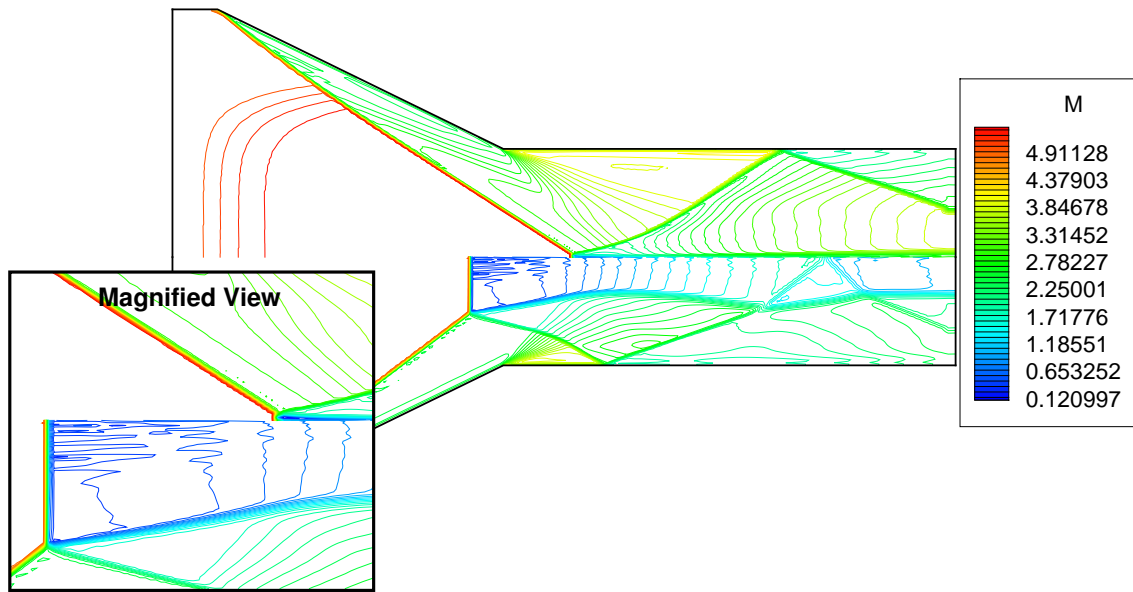
Though transition does not occur, many of the desired goals are realized by this application of an accelerating Lorentz force. Table 4.1 lists the mass-averaged ratios of pressure, temperature, total pressure, and total temperature across the shock system, and includes the maximum temperature in the flowfield, for the RR, MR, and $\mathcal{Q} = 1.0 - 10.0$ solutions. The RR and MR values for pressure and temperature should not be compared to the corresponding values for the accelerating Lorentz force solutions. The variables are sampled as documented above for the mass-averaging of the regular and Mach reflections, but a different procedure is used for the MGD solutions. The variables for the MGD solutions are sampled directly behind the normal shock, well before the solutions reach their maximum static pressure. By sampling close to the shock, the downstream characteristics which vary from interaction parameter to interaction parameter do not effect the results. The compression ratio is smaller than comparable RR and MR values because the region of high pressure is located further downstream of the shock system. The 26° MR and RR experience the highest static pressure directly behind the shock. The maximum

temperature can be compared for all solutions, but the 26° RR T_{max} is larger than theory would predict due to the secondary MR.

Table 4.1   Mass-averaged variable ratios through the shock, interactions ($\theta = 26^o$)

Solution	p_{bs}/p_i	T_{bs}/T_{is}	T_{max}, K	$p_{t_{bs}}/p_{t_i}$	$T_{t_{bs}}/T_{t_i}$
RR	22.18	3.17	437.13	0.283	1.0
MR	19.68	3.63	427.19	0.249	1.0
$Q = 1.0$	13.81	3.58	1114.94	0.346	1.21
$Q = 3.0$	12.78	3.74	4981.32	0.491	1.47
$Q = 5.0$	11.35	3.68	1852.67	0.614	1.61
$Q = 7.5$	10.64	3.60	1444.27	0.743	1.72
$Q = 10.0$	9.47	3.48	1804.07	0.838	1.78

In Table 4.1, as the magnitude of the magnetic field increases, the compression ratio decreases. This parameter is highly affected by the sampling location and this trend is only true of the compression ratios directly behind the shock. Table 4.2 presents a comparison of the pressure and temperature ratios from the inlet to the point of maximum static pressure for the same solutions presented in Table 4.1. The percentage the MR moves as a function of the initial distance between the 26° Mach and regular reflections is also included in the table. The static pressure ratios through the shock system presented in Table 4.2 show the benefit of the accelerating Lorentz force.

Table 4.2   Pressure and temperature ratios through the shock interactions taken at the location of p_{max}

Solution	p_{bs}/p_i	T_{bs}/T_{is}	% Movement of the MR
RR	44.4	4.23	100.0%
MR	28.5	5.79	0.0%
$Q = 1.0$	34.47	6.95	52.45%
$Q = 3.0$	41.01	7.98	96.54%
$Q = 5.0$	45.03	9.89	109.3%
$Q = 7.5$	51.49	8.54	127.74%
$Q = 10.0$	53.33	10.38	136.96%

The 26° Mach reflection has a 64.19% lower maximum compression ratio than the 26° regular reflection. Application of the accelerating Lorentz force for $\mathcal{Q} = 1.0$ increases the maximum compression to 77.64% of the RR value. An increase in the interaction parameter to 10.0 raises the maximum compression ratio beyond the value of the RR by 20.11%. This is a result of the stronger shock system generated by the local $M = 5.44$. This proves the application of MGD is capable of restoring and even increasing the poor compression ratio of a MR.

In Table 4.1, the temperature ratio and corresponding maximum temperature increase until $\mathcal{Q} = 3.0$ and then they decrease. When $\mathcal{Q} = 10.0$, the temperature rise is less than the $\mathcal{Q} = 1.0$ temperature rise. Table 4.2 does not duplicate this trend, with the temperature ratio increasing from $\mathcal{Q} = 1.0$ to $\mathcal{Q} = 10.0$. The discrepancy between the two sets of data is a byproduct of the sampling location. The region where the maximum temperature occurs remains in roughly the same location relative to the shock as the interaction parameter increases. The location of maximum static pressure, where Table 4.2's data originates, moves downstream relative to the shock as the interaction parameter increases. The data for Table 4.2 still captures larger temperature ratios due to the downstream sampling.

The total pressure losses through the shock decrease with increases in the interaction parameter. This trend is due to both the reduction in the size of the MR and the added energy due to the energy interaction term in Eqn. 2.34. The $\mathcal{Q} = 10.0$ solution's Mach stem height is 5% of the 26° MR stem height. This reduction equates to a smaller normal shock and larger oblique shocks making up the shock system. At a set Mach number, an oblique shock has a lower total pressure loss than a normal shock of the same height. The additional increases in total pressure recovery due to the energy interaction term make it possible to actually increase the total pressure through the inlet, if enough energy is added to the system.

The total temperature ratio in Table 4.1 measure how much energy is added to the system. An inlet with no added energy has a total temperature ratio of 1.0.

When the accelerating Lorentz force is applied, the ratio increases by as much as 75% for the $Q = 10.0$ MGD force. Even with this increase, the application of an accelerating Lorentz force has increased the compression ratio across the MR shock system and the total pressure recovery, even increasing both values above the 26° values when $Q \geq 5.0$.

4.4.3 Electric Field Magnitude. Increasing the magnitude of the applied electric field is an alternative approach to creating a larger accelerating Lorentz force (Fig. 3.6) to transition the MR. E_0 is the non-dimensional magnitude of the applied electric field. The electric field is non-dimensionalized by V_0 and B_0, so the nominal $\mathcal{K} = 1.2$ equates to an applied electric field of 2032.23 v/m when $Q = 1.0$. Increasing E_0 above the nominal value proved to be detrimental by overheating the local flow quicker than the flow could be accelerated, lowering the local Mach number. The induced heating of the flow is linear with Q, but increases by the square of E_0. Figure 4.23 shows the converged solution when $\mathcal{K} = 1.8$, an increase of 50%. As expected, the heat addition to the shock system due to the applied force is too great. Even with the accelerated flowfield, the Mach reflection moves upstream. This is the beginning of inlet unstart. This movement raises the total pressure losses and decreases the compression ratio.

With $\mathcal{K} = 2.4$, an applied electric field increase of 100%, the accelerating Lorentz force causes the inlet to unstart as shown in Fig. 4.24. Therefore, $\mathcal{K} = 1.2$ was used in all solutions presented above.

4.5 Magnetogasdynamic Grid Convergence

Throughout this section, it was assumed that magnetogasdynamic effects are independent of grid resolution and follow the same trends as the fluid interactions in Figures 4.3 and 4.6. The coarse mesh was used to investigate preliminary effects for the many parameters in this research, but the actual effects due to the MGD force
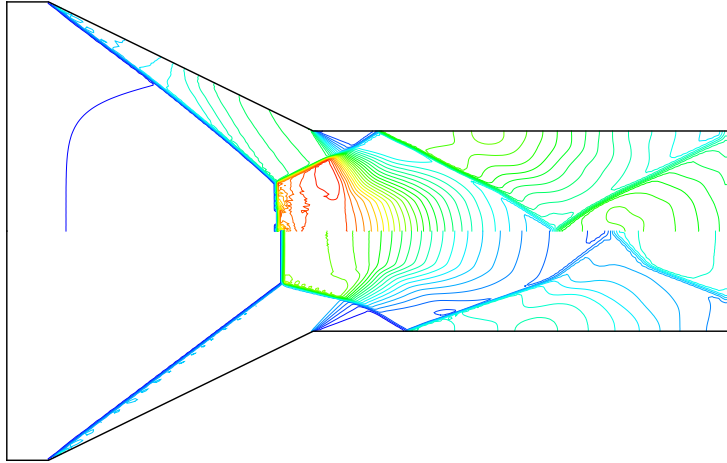
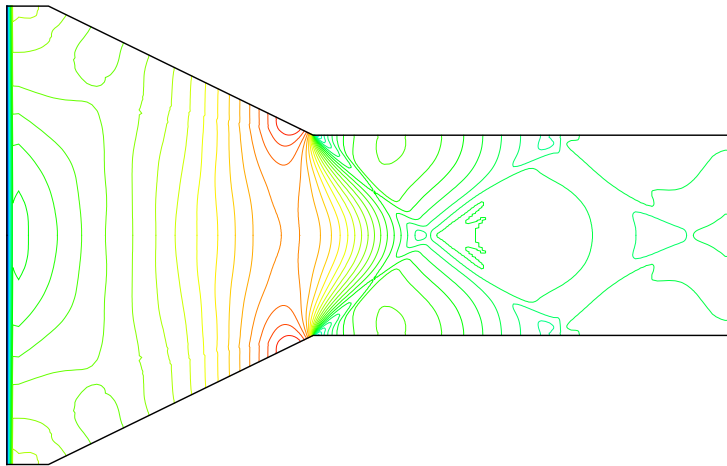Figure 4.23   Pressure contours for $\mathcal{Q} = 1.0$, $\mathcal{K} = 1.8$

Figure 4.24   Pressure contours for $\mathcal{Q} = 1.0$, $\mathcal{K} = 2.4$

were decreased when the solution was resolved on the fine mesh. Figure 4.25 shows the converged solutions after an accelerating Lorentz force is applied with $\mathcal{Q} = 7.5$ to the 26° MR. The MGD force on the bottom has transitioned the coarse mesh MR to a RR. On top, the same force has pushed back and reduced the normal shock on the fine mesh, but a MR remains. When the accelerating MGD force is removed, the coarse mesh transitions to a 26° RR, whereas the fine mesh solution converges to the 26° MR. Both grids illustrate the effect of magnetogasdynamics, but the accelerating Lorentz force does not seem to be grid independent. A detailed magnetogasdynamic grid resolution study is needed to determine grid dependency.
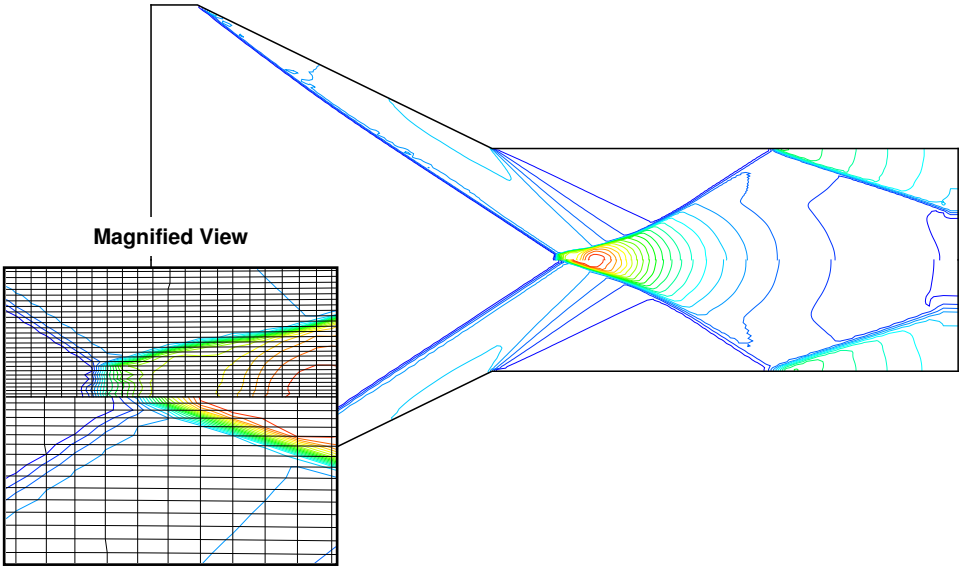

Figure 4.25   Accelerating Lorentz Force with $\mathcal{Q} = 7.5$, coarse mesh on bottom and fine mesh on top, $26^o \times 26^o$

5. Conclusions

The sensitivity of regular reflections and Mach reflections in a double-fin inlet have been examined numerically at $M_\infty = 4.96$. The solutions have been used as the initial conditions for numerical computations with accelerating and decelerating Lorentz forces. These forces have been applied with the intent of determining the sensitivity of the Mach and regular reflections in the dual-solution domain, to transition. The parameters governing application of these magnetogasdynamic forces have been analyzed to determine the optimal application.

The regular reflection has been shown to be very sensitive to a decelerating Lorentz force. Continuous application of this force produced inlet unstart. A decelerating force applied for 2.36×10^{-5} s, but not longer than 8.267×10^{-4} s, transitioned the regular reflection to a Mach reflection after the force had been removed. Continuing the application beyond this time period drove the normal shock upstream and eventually expelled the shock system from the inlet. The careful use of MGD forces in the vicinity of a RR is needed to prevent the detrimental effects of transition to a MR or inlet unstart.

The accelerating Lorentz force has been shown to be very sensitive to the specification of the conductivity. The location of the force determined by the conductivity affects the location of the Mach reflection and the additional effects to the flowfield. The accelerating magnetogasdynamic force as presently applied minimizes, but does not eliminate, the Mach reflection. This yields increased total pressure recovery by the shock system, increased static pressure compression, and downstream movement of Mach stem to a more stable position. Depending on the magnitude of the magnetic field, the accelerating Lorentz force proved capable of increasing the total pressure recovery and the static pressure compression beyond the regular reflection values. This application resulted in a minimal Mach reflection further downstream

than the regular reflection. Therefore, the accelerating force has shown the capability to prevent inlet unstart and increase inlet efficiency.

Future research on the use of MGD to control Mach reflections is needed in three areas. A magnetogasdynamic grid resolution study must be performed to determine grid dependency. The MGD forces have been shown to remain grid dependent for mesh resolutions beyond which fluid interactions have been shown to be grid independent. This research will include an examination of basic magnetogasdynamic relations on grids of varying resolution. The viscous effects of laminar and turbulent boundary layers on the flowfield with accelerating and decelerating Lorentz forces needs to be investigated. The added viscosity could effect the results of the applied force. In addition, the MGD code needs to be modified to calculate the ratio of specific heats based on the temperature. This modification could be as complex as a multi-species reacting flow calculation, or as simple as a table look-up based on the temperature.

Bibliography

1. Anderson Jr., J. D. *Hypersonic and High Temperature Gas Dynamics*. Reston, VA: American Institute of Aeronautics and Astronautics, 1989.

2. Curran, E. T. and S. N. B. Murthy, editors. *Scramjet Propulsion*. Reston, VA: American Institute of Aeronautics and Astronautics, 2000.

3. Gaitonde, D. V. *Development of a Solver for 3-D Non-ideal Magnetogasdynamics*. AIAA Paper 99–3610, June 1999.

4. Gaitonde, D. V. *Three-Dimensional Flow-Through Scramjet Simulation with MGD Energy- Bypass*. AIAA Paper 2003–0172, January 2003.

5. Gaitonde, D. V. and J. Poggie. *Simulation of Magnetogasdynamic Flow Control Techniques*. AIAA Paper 2000–2326, June 2000.

6. Gaitonde, D. V. and J. Poggie. *An Implicit Technique for 3-D Turbulent MGD with the Generalized Ohms Law*. AIAA Paper 2001–2736, June 2001.

7. Gaitonde, D. V. and J. Poggie. *Elements of a Numerical Procedure for 3-D MGD Flow Control Analysis*. AIAA Paper 2002–0198, January 2002.

8. Gaitonde, D. V. and J. Poggie. *Preliminary Analysis of 3-D Scramjet Flowpath with MGD Control*. AIAA Paper 2002–2134, May 2002.

9. Henderson, L. F. and A. Lozzi. "Further experiments on transition of Mach reflection," *Journal of Fluid Mechanics*, *94*:541–559 (1979).

10. Hill, P. G. and C. R. Peterson. *Mechanics and Thermodynamics of Propulsion* (Second Edition). New York: Addison Wesley Publishinc Company, 1992.

11. Hirsch, C. *Numerical Computation of Internal and External Flows, Volume 2*. John Wiley and Sons, 1990.

12. "History of Flight Timeline," *Celebrating the Evolution of Flight... 1903-2003...And Beyond* AIAA Website, (2004). 24 January 2004 http://www.flight100.org/history_intro.html.

13. Hornung, H. G., et al. "Transition to Mach Reflection of Shock Waves in Steady and Pseudosteady Flow With and Without Relaxation," *Journal of Fluid Mechanics*, *90*:541–560 (February 1979).

14. Hornung, H. G. and J. R. Taylor. "Transition to Mach Reflection of Shock Waves Part 1. The Effect of Viscosity on the Pseudosteady Case," *Journal of Fluid Mechanics*, *123*:143–153 (October 1982).

15. Hughes, W. F. and F. J. Young. *The Electromagnetodynamics of Fluids* (Reprint Edition). Malabar, FL: Robert E. Krieger Publishing Company, 1989.

16. "HyShot program secures place in flight history," *UQ News Online* University of Queensland, Austrailia, Website, (2002). 10 February 2004 http://www.uq.edu.au/news/index.phtml?article=3469.

17. Ivanov, M. S., et al. *Numerical and Experimental Study of 3D Steady Shock Wave Interactions*. AIAA Paper 2001–0740, January 2001.

18. Ivanov, M. S., et al. "Experiments on Shock Wave Reflection Transition and Hysteresis in Low-Noise Wind Tunnel," *Physics of Fluids*, *15*(6):1807–1810 (May 2003).

19. Ivanov, M. S., et al. *Real Gas Effects on the Transition Between Regular and Mach Reflections in Steady Flows*. AIAA Paper 98–0877, January 1998.

20. Ivanov, M. S., et al. "Numerical Analysis of Shock Wave Reflection Transition in Steady Flows," *AIAA Journal*, *36*(11):2079–2086 (November 1998).

21. Johnsen, F. A., "Second X-43 Takes a Ride Under the B-52," *Dryden Flight Research Center* NASA DRFC Website, (2004). 10 February 2004 http://www.dfrc.nasa.gov/Current_News/X-43_26Jan2004.html.

22. Kuranov, A. and E. Sheikin. *The Potential of MHD Control for Improving Scramjet Performance*. AIAA Paper 99–3535, June 1999.

23. Kuranov, A. and E. Sheikin. *MHD Control on Hypersonic Aircraft under "AJAX" Concept. Possibilites of MHD Generator*. AIAA Paper 2002–0490, January 2002.

24. "Lockheed SR-71A," *United States Air Force Museum* USAF Museum Website, (2004). 24 January 2004 http://www.wpafb.af.mil/museum/modern_flight/mf35.htm.

25. Macheret, S., et al. "Magnetohydrodynamic Control of Hypersonic Flows and Scramjet Inlets Using Electron Beam Ionization," *AIAA Journal*, *40*(1):74–81 (January 2002).

26. McMullan, R. J. *Numerical Boundary Conditions Simulating the Interaction Between Upstream Disturbances and an Axial Compressor*. PhD dissertation, North Carolina State University, Raleigh, NC, August 2002.

27. Mitchner, M. and C. Kruger. *Partially Ionized Gases*. John Wiley and Sons, 1973.

28. Roe, P. L. "Approximate Riemann Solvers, Parameter Vectors and Difference Schemes," *Journal of Computational Physics*, *43*(2):357–372 (October 1981).

29. Schmisseur, J. D. and D. V. Gaitonde. *Numerical Investigation of New Topologies in Strong Crossing Shock-Wave/Turbulent Boundary-Layer Interactions*. AIAA Paper 2000–0931, January 2000.

30. Schmisseur, J. D. and D. V. Gaitonde. *Numerical Simulation of Mach Reflection in Steady Flows*. AIAA Paper 2001–0741, January 2001.

31. Tannehill, J. C., et al. *Computational Fluid Mechanics and Heat Transfer* (Second Edition). Philadelphia: Taylor and Francis, 1997.

32. Vatsa, V. N., et al. *Navier-Stokes Computations of a Problate Spheroid at Angle of Attack*. AIAA Paper 87–2627–CP, August 1987.

33. White, F. *Viscous Fluid Flow*. Boston: McGraw Hill, 1991.

34. Yan, H., et al. *Laser Energy Deposition in Intersecting Shocks*. AIAA Paper 2002–2729, June 2002.

35. Yan, H., et al. *Localized Flow Control by Laser Energy Deposition Applied to Edney IV Shock Impingement and Intersecting Shocks*. AIAA Paper 2003–0031, January 2003.

Vita

Captain Brian E. Earp was born in Charlottesville, VA. He was raised in Louisville, Kentucky and graduated from Seneca High School in 1995. He entered undergraduate studies at the United States Air Force Academy in Colorado Springs, CO, where he graduated with a Bachelor of Science degree in Aeronautical Engineering and was commissioned in June of 1999.

His first assignment was at the University of Louisville in Louisville, KY, as an Assistant Regional Director of Admissions, known simply as a Goldbar. After a year serving at AFROTC Detachment 152, he was assigned to the Access to Space Office at Edwards AFB, CA, in September of 2000. While at Edwards he worked as a Developmental Aeronautical Engineer with the Air Force Research Laboratory and NASA, including work on many of NASA's experimental vehicles. He attended the Aerospace Vehicle Test Course at the United States Air Force Test Pilot School in October of 2001.

In August 2002, he entered the Aeronautical Engineering program at the Graduate School of Engineering and Management, Air Force Institute of Technology. His academic focus areas were Computational Fluid Mechanics, Aerodynamics, and Propulsion. Upon graduation, he will be assigned to the Air Force Research Laboratory's Air Vehicles Directorate at Wright-Patterson AFB, OH, where he will continue his work with the Computational Aerodynamics Branch in hypersonic computational fluid dynamics.

1. REPORT DATE *(DD–MM–YYYY)*	2. REPORT TYPE	3. DATES COVERED *(From — To)*
23–03–2004	Master's Thesis	Sep 2002 – Mar 2004

4. TITLE AND SUBTITLE

MAGNETOGASDYNAMIC FLOW CONTROL OF A MACH REFLECTION

5a. CONTRACT NUMBER

5b. GRANT NUMBER

5c. PROGRAM ELEMENT NUMBER

6. AUTHOR(S)

Earp, Brian E., Captain, USAF

5d. PROJECT NUMBER

2003–029

5e. TASK NUMBER

5f. WORK UNIT NUMBER

7. PERFORMING ORGANIZATION NAME(S) AND ADDRESS(ES)

Air Force Institute of Technology
Graduate School of Engineering and Management
2950 Hobson Way
WPAFB OH 45433-7765

8. PERFORMING ORGANIZATION REPORT NUMBER

AFIT/GAE/ENY/04-M07

9. SPONSORING / MONITORING AGENCY NAME(S) AND ADDRESS(ES)

AFRL/VAAC
Dr. Datta V. Gaitonde
2210 8th Street, Rm 225
WPAFB OH 45433-7512 (937) 904–4031

10. SPONSOR/MONITOR'S ACRONYM(S)

11. SPONSOR/MONITOR'S REPORT NUMBER(S)

12. DISTRIBUTION / AVAILABILITY STATEMENT

APPROVAL FOR PUBLIC RELEASE; DISTRIBUTION IS UNLIMITED.

13. SUPPLEMENTARY NOTES

14. ABSTRACT

Two-dimensional regular and Mach reflections have been studied in the Mach 4.96 dual-solution domain for a 25° and 26° double-fin inlet. The steady-state computational Mach and regular reflections were subjected to magnetogasdynamic forces to determine whether these forces could be used as a possible flow control mechanism. The numerical code employed for this research solved the inviscid Euler equations with added source terms for the ponderomotive force and accompanying energy interactions. The 25° regular reflection was determined to be extremely sensitive to a decelerating Lorentz force. Transient application of the force led to the transition of the regular reflection to a Mach reflection, increasing the total pressure losses and decreasing the compression ratio. Sustained application of the force resulted in inlet unstart. An accelerating Lorentz force was also examined with the goal of transitioning the 26° Mach reflection to a more efficient regular reflection. The location of the accelerating force and the parameters governing its magnitude were examined. Such forces push the Mach reflection back to a more stable location and reduce the Mach stem height. For the interaction parameters considered, fully regular reflections were not obtained. However, the accelerating Lorentz force proved capable of increasing the total pressure recovery and the static pressure compression beyond the regular reflection values.

15. SUBJECT TERMS

Mach Reflection; Regular Reflection; Shock Reflection; Magnetogasdynamics; Flow Control; Plasma

16. SECURITY CLASSIFICATION OF:			17. LIMITATION OF ABSTRACT	18. NUMBER OF PAGES	19a. NAME OF RESPONSIBLE PERSON
a. REPORT	b. ABSTRACT	c. THIS PAGE			Richard J. McMullan, Maj, USAF (ENY)
U	U	U	UU	98	19b. TELEPHONE NUMBER *(include area code)* (937) 255–3636, ext 4559